Geochemistry Geophysics Geosystems G3
AN ELECTRONIC JOURNAL OF THE EARTH SCIENCES
Published by AGU and the Geochemical Society

Article
Volume 9, Number 9
30 September 2008
Q09O12, doi:10.1029/2008GC001970
ISSN: 1525-2027

Magmatic and tectonic extension at mid-ocean ridges: 2. Origin of axial morphology

Garrett Ito
Department of Geology and Geophysics, SOEST, University of Hawai'i at Manoa, 1680 East-West Road, POST 810, Honolulu, Hawaii 96822, USA (gito@hawaii.edu)

Mark D. Behn
Department of Geology and Geophysics, Woods Hole Oceanographic Institution, 360 Woods Hole Road, Mail Stop 22, Woods Hole, Massachusetts 02543, USA (mbehn@whoi.edu)

[1] We investigate the origin of mid-ocean ridge morphology with numerical models that successfully predict axial topographic highs, axial valleys, and the transition between the two. The models are time-dependent, simulating alternating tectonic and magmatic periods where far-field extension is accommodated by faulting and by magmatism, respectively. During tectonic phases, models predict faults to grow on either side of the ridge axis and axial height to decrease. During magmatic phases, models simulate magmatic extension by allowing the axial lithosphere to open freely in response to extension. Results show that fault size and spacing decreases with increasing time fraction spent in the magmatic phase F_M. Magmatic phases also simulate the growth of topography in response to local buoyancy forces. The fundamental variable that controls the transition between axial highs and valleys is the "rise-sink ratio," $(F_M/F_T)(\tau_T/\tau_M)$, where F_M/F_T is the ratio of the time spent in the magmatic and tectonic periods and τ_T/τ_M is the ratio of the characteristic rates for growing topography during magmatic phases $(1/\tau_M)$ and for reducing topography during tectonic phases $(1/\tau_T)$. Models predict the tallest axial highs when $(F_M/F_T)(\tau_T/\tau_M) \gg 1$, faulted topography without a high or valley when $(F_M/F_T)(\tau_T/\tau_M) \sim 1$, and the deepest median valleys when $(F_M/F_T)(\tau_M/\tau_T) < 1$. New scaling laws explain a global negative correlation between axial topography and lithosphere thickness as measured by the depths of axial magma lenses and microearthquakes. Exceptions to this trend reveal the importance of other behaviors such as a predicted inverse relation between axial topography and spreading rate as evident along the Lau Spreading Center. Still other factors related to the frequency and spatial pervasiveness of magmatic intrusions and eruptions, as evident at the Mid-Atlantic and Juan de Fuca ridges, influence the rise-sink-ratio $(F_M/F_T)(\tau_T/\tau_M)$ and thus axial morphology.

Components: 12,871 words, 10 figures, 2 tables.

Keywords: mid-ocean ridge; magmatism; seafloor spreading; faulting; rifting.

Index Terms: 1032 Geochemistry: Mid-oceanic ridge processes (3614, 8416); 8178 Tectonophysics: Tectonics and magmatism; 8004 Structural Geology: Dynamics and mechanics of faulting (8118).

Received 30 January 2008; **Revised** 1 July 2008; **Accepted** 30 July 2008; **Published** 30 September 2008.

Ito, G., and M. D. Behn (2008), Magmatic and tectonic extension at mid-ocean ridges: 2. Origin of axial morphology, *Geochem. Geophys. Geosyst.*, *9*, Q09O12, doi:10.1029/2008GC001970.

Theme: Formation and Evolution of Oceanic Crust Formed at Fast Spreading Rates
Guest Editors: D. A. H. Teagle and D. Wilson

1. Introduction

[2] The contrast in mid-ocean ridge morphology between deep (1–2 km) axial valleys with heavily faulted flanks, and highstanding, axial ridges with minimal fault relief ($\leq\sim10^2$ m) has been a long-standing topic of interest [e.g., *Macdonald*, 1982, 1986]. Slow spreading (20–30 km/Ma, full rate) ridges such as the Mid-Atlantic Ridge (MAR) typically form axial valleys; fast spreading (>70 km/Ma) ridges typically form axial highs; and ridges spreading at intermediate rates such as the Galapagos Spreading Center (GSC) and Southeast Indian Ridge (SEIR) display the full range of morphologies from valleys, to faulted flat topography, faulted highs, and minimally faulted highs (Figure 1). Axial high topography probably originates from the buoyancy of low-density, partially molten material below the axis and relatively small nonlithostatic stresses [*Madsen et al.*, 1984; *Wang and Cochran*, 1993; *Magde et al.*, 1995; *Buck*, 2001; *Shah and Buck*, 2001]. Axial valleys most likely reflect large nonlithostatic stress that both depresses the axis and causes the valley flanks to be uplifted [e.g., *Tapponnier and Francheteau*, 1978; *Lin and Parmentier*, 1989; *Chen and Morgan*, 1990a, 1990b; *Lin and Parmentier*, 1990].

[3] Seminal work by *Chen and Morgan* [1990a, 1990b] and *Phipps Morgan and Chen* [1993a, 1993b] led to the widely believed concept that axis morphology is a direct consequence of the thickness of the axial lithosphere, which in turn is controlled by the balance of heat added primarily by magma delivered to the axis and heat lost to the seafloor. The large magma flux at fast spreading ridges and hot spot-influenced, intermediate-spreading ridges [*Chen and Phipps Morgan*, 1996; *Chen and Lin*, 2004] is predicted to produce a thin lithosphere and hot lower crust. These researchers proposed that the hot, partially molten lower crust supplies the buoyancy to uplift the axis but is too weak to transmit stress from the stronger, peridotite mantle and cause the overlying lithosphere to break. In contrast, the smaller magma flux at slow-spreading ridges or some intermediate-spreading ridges promotes a thick lithosphere that is well coupled to the strong upper mantle. A thick section of lithosphere is therefore hypothesized to be subject to large stresses, allowing it to support a deep axial valley and large faults. *Poliakov and Buck* [1998] provide a nice review of this framework of understanding and extend it by examining some of the first numerical models that simulated spontaneous formation and evolution of normal faults.

[4] While extension at the ridge axis is known to occur both tectonically and magmatically [e.g., see *Carbotte and Macdonald*, 1994; *Escartín et al.*, 1999, and references therein] only recently has this tectonomagmatic cycle been examined in numerical models. *Buck et al.* [2005], for example, simulated the injection of dikes at the axis, which accommodate a fraction M of the total rate of seafloor spreading. They predicted faulted axial valleys when $M < 1$ and axial highs when $M = 1$. *Behn et al.* [2006] simulated the accretion of ''blade-like'' dikes (widths that increase with depth) and showed that there is likely a feedback between axial valley topography and the frequency of dike injection.

[5] Our companion paper [*Behn and Ito*, 2008, hereafter referred to as Paper 1] presents an in-depth study of the mechanics of faulting at mid-ocean ridges. Supporting the results of *Buck et al.* [2005], Paper 1 shows that M is a key parameter controlling fault evolution, with lower values leading to larger more widely spaced faults. Lithosphere structure also influences faulting. Contrary to some previous views, we found that thicker lithosphere (with the same fractional rate of off-axis thickening) actually leads to smaller, not larger, fault size and spacing. Lower rates of thickening away from the axis, however, have the opposite effect. The inference made is that large M and rapid off-axis cooling of the crust promotes small, closely spaced faults at magmatically robust ridges (e.g., fast to intermediate spreading) whereas lower M with more subdued off-axis lithosphere thickening, since it is already thick beneath the axis, leads to the larger, more widely spaced faults

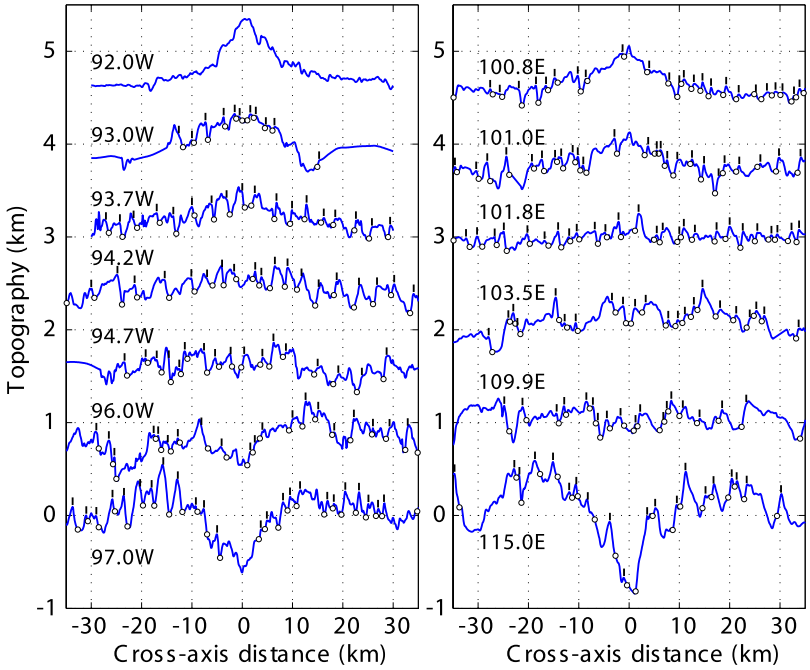

Figure 1. Bathymetry profiles crossing the (a) Galapagos Spreading Center (half spreading rate increasing from bottom to top between 23.3 and 26.4 km/Ma) and (b) Southeast Indian Ridge (spreading rates 35.3–35.5 km/Ma from bottom to top) at locations labeled. Vertical lines show picks of tops of faults; open circles show picks of bottom of faults. Data from multibeam bathymetry are available at http://www.geomapapp.org/ and *Cochran et al.* [1997] and *Sinton et al.* [2003].

at magmatically starved ridges (e.g., intermediate to slow spreading).

[6] Paper 1 also reveals a key limitation of simulating the tectonomagmatic cycle with the single parameter M, which assumes an infinitesimally small time interval between tectonic and magmatic events. Specifically, this approach results in nonlithostatic tension at the ridge axis sufficient to continually fault the lithosphere for all cases in which $M < 1$. Consequently, all simulations with $M < 1$ in Paper 1 (and in the work of *Buck et al.* [2005]) predict axial valleys of varying depths and no model predicts faulted transitional or faulted axial high topography such as that seen in Figure 1.

[7] The purpose of this paper is to define the primary factors that influence faulting as well as the characteristic morphologies of mid-ocean ridges: axial valleys, axial highs, and the transition between them. Our calculations simulate time-dependent crustal accretion and tectonism by specifying a time fraction F_M that the axis is in a magmatic phase compared to the whole tectonomagmatic cycle. Individual effects of various factors including F_M, the duration of the tectonomagmatic cycle, lithosphere thickness, and spreading rate are quantified. We will show that the transition between axial high and median valley morphology does not depend on the amount of lithospheric coupling with the stiff mantle [*Chen and Morgan*, 1990a, 1990b] but rather on the "rise-sink ratio" of the crust, $(F_M/F_T)(\tau_T/\tau_M)$, where $F_T = 1 - F_M$ is the time fraction in the amagmatic or tectonic period and τ_T/τ_M is the ratio of the rates at which the ridge axis rises during magmatic phases and sinks during tectonic phases. Variables such as spreading rate and axial lithosphere thickness are shown to affect axial morphology through their influence on the "rise-sink ratio."

2. Method

2.1. Mechanical Model

[8] Full details of the numerical methods are described in Paper 1; here we outline the most salient similarities and specify the particular differences incorporated in this study. The mathematical variables are listed in Table 1. To simulate two-dimensional (2-D) lithosphere accretion, faulting, and topography we numerically solved the conservation equations of mass and momentum for a visco-elasto-plastic material (Figure 2). We used the same hybrid finite element method (FLAC) and rheological formulations as in

Table 1. Summary of Variables Used

Variable	Meaning	Value(s)	Units
C	scaling constant in equation (7)	7.92×10^{14}	Nm
F_M	P_M/P, time fraction of magmatic period	0.7–1	—
F_T	$P_T/P = (1 - F_M)$ time fraction of tectonic period	0–0.3	—
H_{400}	depth of 400°C-isotherm beneath the axial seafloor	1.3–4.0	km
h	long wavelength axial height relative to adjacent seafloor		km
h_M	axial height in isostatic equilibrium		km
M	fraction magmatic extension		—
P_M	time period of magmatic phase		ka
P_T	time period of tectonic phase		ka
P	$P_M + P_T$, duration of tectonomagmatic cycle	10–502.5	ka
w_T	depth of deepest axial valley		km
Δx	fault heave		km
ΔS	average fault spacing		km
U	half spreading rate		km/Ma
x_{AF}	furthest distance from axis a fault remains active	10–75	km
z_{400}	depth of 400°C isotherm below seafloor		km
η_M	model maximum viscosity in accretion zone		Pa s
τ_T	timescale for reducing topography during tectonic episodes		ka
τ_M	timescale for topographic growth during magmatic periods		ka

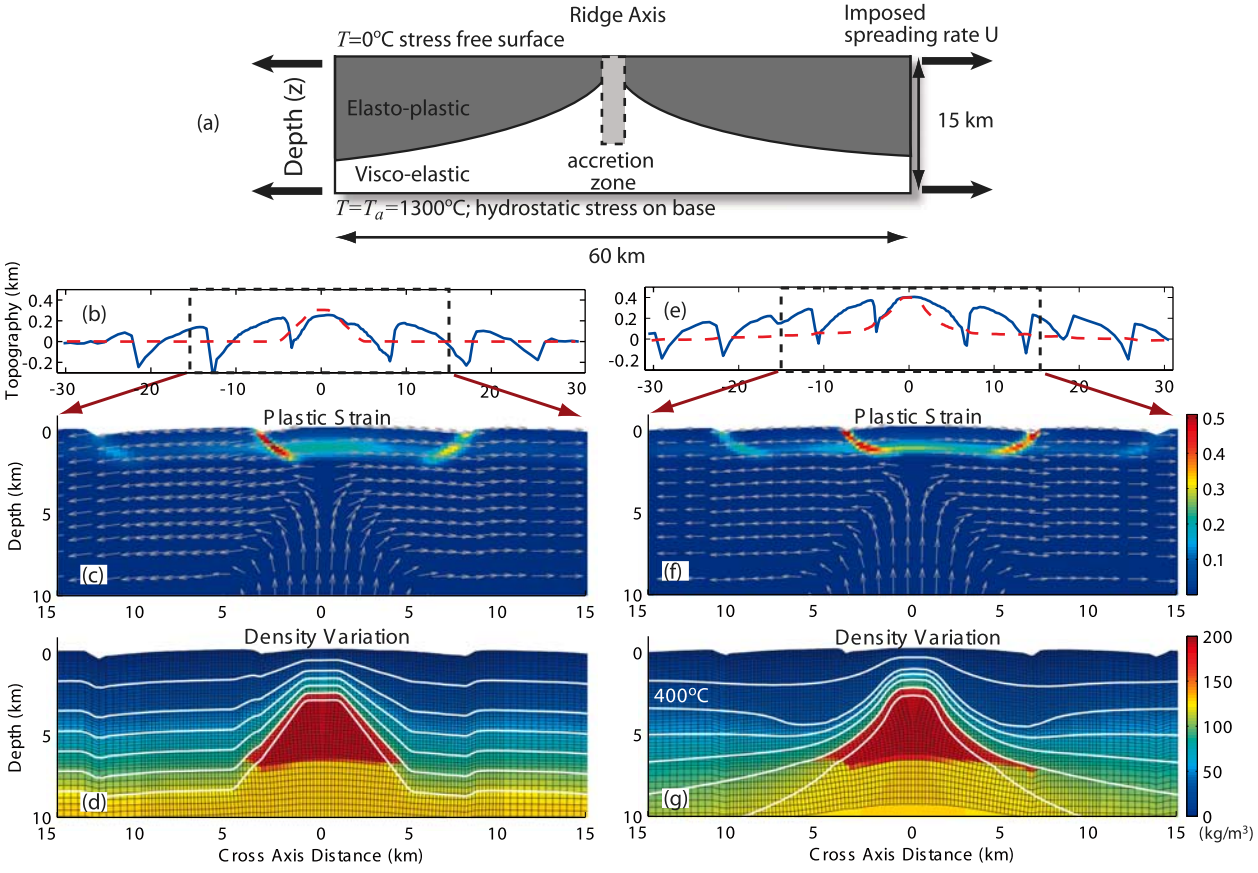

Figure 2. (a) Model geometry and boundary conditions and example calculations for cases in which thermal structure is (b)–(d) imposed and (e)–(g) computed. In each case, depth to the 400°C isotherm is H_{400} = 1.3 km, time fraction of the magmatic phase is F_M = 0.8, and half spreading rate is U = 25 km/Ma. Figures 2b and 2e show surface topography (solid) and isostatic topography (dashed); Figures 2c and 2f show accumulated plastic strain (colors) and flow direction (arrows); and Figures 2d and 2g panels show density structure (colors) and temperature (contoured every 200°C).

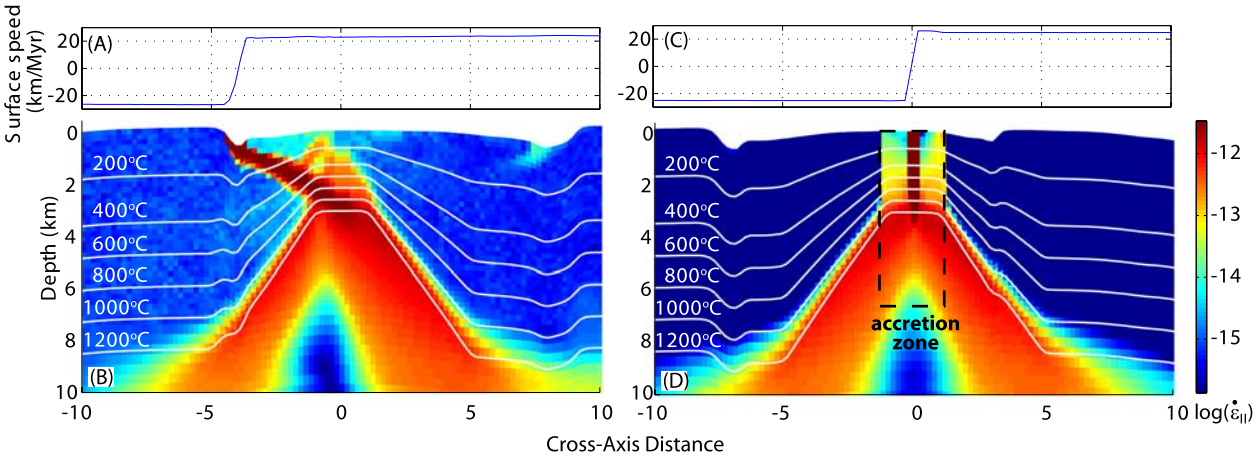

Figure 3. (a and c) Horizontal speed of the surface; (b and d) strain rate (as second invariant of the strain rate tensor). (left) During an amagmatic phase, extension is accommodated along a single fault. (right) During the magmatic phase extension is accommodated within the accretion zone. Figures 3a–3d are different time steps of the same model run with H_{400} = 1.3 km, F_M = 0.8, and U = 25 km/Ma (same as in Figures 2b–2d).

Paper 1 and developed recently by Buck, Lavier, and Poliakov [e.g., *Poliakov and Buck*, 1998; *Lavier and Buck*, 2002; *Buck et al.*, 2005]. The model domain was rectangular and centered on the ridge axis (Figure 2). In most cases the domain was 60 km wide by 15 km deep with the smallest grid elements (0.2 × 0.2 km) located within a distance of 1 × 1 ≤ 10 km of the axis and a depth $z \leq 7$ km. Outside of this region, grid size increased toward the bottom corners of the model box to a maximum size of 0.8 × 0.8 km. For calculations with the thickest lithosphere (subaxial depth of 400°C isotherm being H_{400} = 4 km, see section 2.3), we required less resolution (i.e., faults were more widely spaced and extended deeper) as well as a larger box to encompass the lithosphere's larger flexural wavelength and full temperature structure. For these calculations, the box was 100 × 20 km with minimum grid dimensions of 0.33 × 0.33 km within $x \leq 12$ km of the ridge and $z \leq 9$ km.

[9] Faulting was simulated with elastoplasticity, using Mohr-Coulomb failure criteria. Strain localization was promoted by reducing cohesion (shear stress for brittle failure at zero pressure) as a linear function of plastic strain. Cohesion was reduced linearly from 44 MPa to 2 MPa over a time that is well less than the duration individual faults remained active. For most of our calculations (i.e., $F_M \leq 0.9$) this condition was met by reducing the cohesion over a total fault displacement of ~0.3 km (i.e., plastic strain of 0.39 for a grid spacing of 0.2 km). Calculations for higher F_M, required a cohesion weakening over 0.1–0.2 km of slip (plastic strain of 0.10–0.25). Our results were insensitive to the rate of weakening with plastic strain, provided that faults weakened completely and over a time that was shorter than the specified fault healing time (320 ka).

[10] Seafloor spreading was simulated by imposing horizontal motion on the left and right sides of the model box at a rate of U which defines the half-spreading rate. The top boundary was stress free and the base was maintained at the hydrostatic stress (which changes as the base moves up and down with the Lagrangian grid). The density contrast at the surface was set to that between mantle and water (2300 kg/m^3). This treatment is equivalent to the simplifying assumption that the crust, which is less dense than mantle, is of uniform thickness everywhere at each point beneath the seafloor.

2.2. Method of Simulating the Tectonomagmatic Cycle

[11] In contrast to Paper 1 in which a fraction M of the total spreading rate was accommodated by magmatism at all times, in this study, we explicitly simulated temporal variations in magmatism. Amagmatic or tectonic periods involved zero magmatic accretion (i.e., M = 0) for a time period P_T. During tectonic periods, tension built in the lithosphere, the ridge axis was drawn downward, and faults formed and grew (Figures 3a–3b). Magmatic periods were simulated by allowing the two columns of elements that define the ridge axis to open freely within the crust ($z \leq 7$ km) in response to plate spreading (Figures 3c–3d). This was done by removing all nonlithostatic stresses in these elements at each time step. In addition, magmatic

periods involved limiting viscosity to a maximum of η_M within the magmatic zone of $1 \times 1 \leq 2$ km. When the parameter η_M was large (10^{27} Pa s), the rheology was not perturbed compared to the pressure-temperature dependence that defined the basic rheology (i.e., the rheology everywhere else and in the whole model during tectonic phases). When $\eta_M \leq 10^{20}$ Pa s, the whole magmatic zone deformed viscously and axial topography tended to rise in response to local buoyancy forces. Parameter η_M does not represent a laboratory-based rheological property but rather is a parameter that accounts for the time- and space-integrated effects of magmatic intrusions and eruptions, which both weaken and thicken the crust. Here η_M controls the characteristic timescale τ_M or the rate $1/\tau_M$ that it takes magmatism to build topography toward the level of isostatic equilibrium (e.g., Figure 2).

[12] The model magmatic periods represent times when the liquid magma volume that is present within or transported through the crust is high enough to minimize nonlithostatic stresses and to cause positive growth of topographic. These periods include but are not limited to times of active eruptive episodes. Correspondingly, tectonic periods represent times in which magma volume and/or flux are relatively low such that nonlithostatic tension increases and topographic growth is negative. Magmatic periods last a time P_M, tectonic periods last P_T. Thus, the whole tectonomagmatic cycle lasts $P = (P_M + P_T)$, and the corresponding time fractions of magmatic and tectonic periods are $F_M \equiv P_M/P$ and $F_T \equiv P_T/P = (1 - F_M)$, respectively. We examined values of F_M ranging from 0.7 to 1, which is consistent with estimates of spreading rate fractions of $M = 0.7–0.9$ at heavily faulted ridges from studies of seismic moment release [*Solomon et al.*, 1998] and fault relief [*Escartín et al.*, 1999].

[13] These strongly time-dependent calculations required dynamic adjustments of model time steps to maintain quasi-static equilibrium. This was done by reducing time steps when the maximum normalized acceleration (acceleration of a node divided by the acceleration that would be caused by the sum of the forces on the node if they acted in the same direction) exceeded 0.03. This adjustment was typically needed after remeshing steps and during the transition between tectonic and magmatic phases. In so doing, time steps typically varied between $\sim 10^{-5}$ and $\sim 10^{-4}$ ka with a total of $30–40 \times 10^6$ steps needed for a typical calculation simulating 1.3 Ma. Another measure that was taken to stabilize solutions was to impose the transition from the tectonic to magmatic phase gradually over 1 ka in model time. By reducing both the nonlithostatic stresses in the central dike elements and the log of the viscosity cutoff in the magmatic zone (toward η_M) linearly over this time, the large axial stresses that had built up during the tectonic phase decayed gradually toward those present during the magmatic phase. The transition from the magmatic back to the tectonic phase occurred over a single time step.

2.3. Temperature and Density Structure

[14] Temperatures are important in controlling thermal buoyancy and rheology as described in Paper 1. The thermal structure of our models includes a thin lithosphere beneath the axis that rapidly thickens on either side of the axis, consistent with geophysical studies of fast-intermediate spreading ridges [*Toomey et al.*, 1994; *Vera and Diebold*, 1994; *Dunn et al.*, 2000; *Crawford and Webb*, 2002; *Canales et al.*, 2006], and segment centers of slow-spreading ridges [*Dunn et al.*, 2005]. We used two ad hoc approaches to simulate such a thermal structure. The first approach was to impose temperatures as a function of distance x from the axis and depth z below the local seafloor (Figure 2d). In this case, temperature increases linearly from 0°C at $z = 0$ to 400°C at $z = z_{400}$ (i.e., depth of 400°C isotherm), then to a maximum of 1300°C between $z = z_{400}$ and $z = 2.5z_{400}$, and remains uniform at 1300°C at greater depths. Depth z_{400} varies with distance x from the axis, being shallowest for $1 \times 1 \leq 1$ km, increasing by 2.33 km at $1 \times 1 = 5$ km, and then remaining at a constant, maximum value for $1 \times 1 > 5$ km. The minimum of z_{400} for $1 \times 1 \leq 1$ km defines the parameter H_{400}, axial lithosphere thickness, for which we consider values of 1.3, 1.8, 2.5, and 4.0 km. This range implies lithosphere (i.e., the material that faults) with a minimum thickness slightly larger than the ~1 km values determined from the shallowest axial magma lens at fast spreading ridges [e.g., *Detrick et al.*, 1987] and a maximum thickness within the range of the slow-spreading Mid-Atlantic Ridge based on the deepest of microearthquakes (3–9 km) [*Toomey et al.*, 1988; *Kong et al.*, 1992; *Wolfe et al.*, 1995; *Barclay et al.*, 2001]. We will refer to these models as cases with imposed thermal structure.

[15] The second approach simulated a more realistic structure by solving the time-dependent, advection-diffusion equation for temperature with heat sources (Figure 2g and equation (2) of Paper 1).

Temperatures at the surface were maintained at 0°C and set equal to the steady state solution for a cooling half-space at the depths coinciding to the model base, subject to a maximum of 1300°C. Insulating boundaries were imposed on the left and right sides of the box. The initial conditions for cases with $F_M = 1.0$ was the steady state solution of a cooling half-space. The initial condition for cases with $F_M < 1.0$ was the final solution of the appropriate case with $F_M = 1.0$. As in Paper 1, we parameterized the effects of hydrothermal circulation by scaling the thermal diffusivity by a factor Nu [e.g., *Phipps Morgan and Chen*, 1993a, 1993b]. To achieve the values of H_{400} and similar variations in z_{400} as in our fixed temperature cases above we set $Nu = Nu_0$ for $1 \times 1 \leq 0.5$ km, $Nu = 10$ for $1 \times 1 = 4–5$ km, $Nu = 1.0$ (no hydrothermal circulation) for $1 \times 1 > 8$ km, and changed Nu linearly between the specified ranges of x. Values for Nu_0 of 5.6 and 8.5 combined with the thermal and latent heat flux associated with 7 km of crust accreting at the spreading rate yielded H_{400} of 1.3 and 1.8 km, similar to the first two cases with imposed thermal structure. For simplicity, the thermal effects of magmatism where held constant in time; they did not vary between tectonic and magmatic phases. We will refer to these thermal models as cases with computed thermal structure.

[16] The other contribution to density is magma in the lower crust. Following previous studies [e.g., *Sinton and Detrick*, 1992; *Phipps Morgan and Chen*, 1993a, 1993b; *Shah and Buck*, 2001; *Maclennan et al.*, 2004] we assumed that crust at temperatures above the magma solidus is partially molten. Thus between the 1000°C isotherm and $z =$ 7 km we imposed a density reduction of 60 kg/m^3, which is equivalent to that associated with 20% melt that is 300 kg/m^3 less dense than the fully solid gabbro. This density is the same for all model runs and therefore should be considered a reference value, probably near the upper bound for estimates beneath the East Pacific Rise [*Dunn et al.*, 2000; *Crawford and Webb*, 2002].

2.4. Measuring Long-Wavelength Height and Fault Characteristics

[17] The main output of our models is surface topography. Because repeated regridding of the Lagrangian mesh caused the sharp topography of faults to diffuse with time, we tracked topography using passive tracers. These tracers were initially placed along the surface of the model at 0.1 km spacing and then added at the axis and removed from the two sides of the model during the simulation of seafloor spreading. Velocities of each particle were computed by linearly interpolating the velocities between the finite element nodes; positions were computed using upwind differencing in time.

[18] From the predicted topography (example shown in Figure 2), we had to separate the short-wavelength component due to faulting and the long-wavelength component associated with axial morphology. Fault scarps were identified as the steepest features that dip toward the axis in Figure 2. The two key fault characteristics are fault spacing ΔS, which was measured by the distance between the bases of the faults, and fault heave Δx, which was measured by the horizontal offset between the fault bases and peaks. To quantify the long-wavelength topography associated with axial highs or valleys, we measured the height of the axis above the surrounding seafloor, h, using two methods. Method 1 measured axis height h_1 as the difference between the axis depth and the mean depth of the two fault peaks that were most distal from the axis on each plate. Method 2 measured axis height h_2 as the difference between the axis depth and the mean depth of the shallowest fault peaks on each side of the axis. Axial height h was defined as $h = h_1$ when $h_1 > 0$ and $h = h_2$ when $h_1 < 0$. Thus, h measures the height of axial topographic highs when $h = h_1 > 0$ and the depth of axial valleys when $h = h_2 < 0$ (h_2 is always less than h_1).

3. Results

3.1. General Model Predictions

[19] Calculations were integrated in time so that all of the seafloor was created during the model runs (e.g., 1300 ka for $U = 25$ km/Ma). Like in Paper 1, our simulations typically predict one fault to form on one side of the axis and remain active to a maximum distance x_{AF}, at which point a new fault forms on the opposite plate. The axis tends to rise during magmatic phases and sink during tectonic phases in a saw-tooth pattern in time with amplitudes typically 0.01–0.02 km. Below we show how and why fault characteristics (i.e., spacing ΔS and heave Δx) and long-wavelength topography h are controlled by five key parameters: (1) P, duration of the tectonomagmatic cycle, (2) F_M, magmatic time fraction, (3) H_{400}, axial lithosphere thickness, (4) η_M, which is proportional to the rate $1/\tau_M$ of topographic growth during magmatic phases, and (5) U, half-spreading rate.

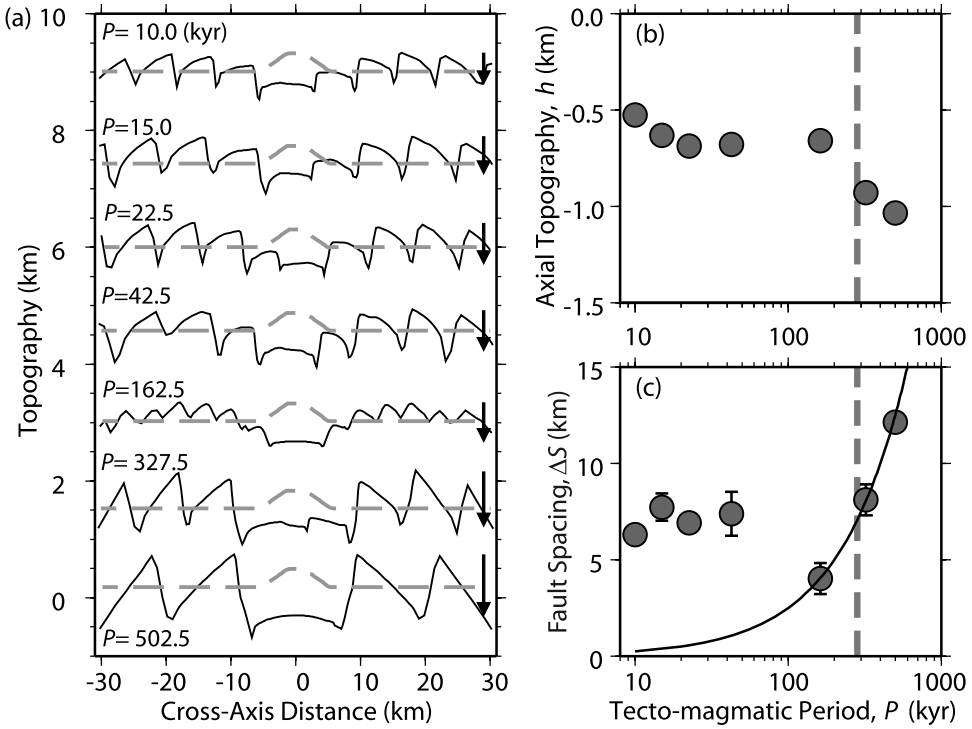

Figure 4. (a) Bathymetry profiles predicted for cases in which U = 25 km/Ma, $\eta_m = 1 \times 10^{27}$ Pa s, F_M = 0.8, imposed thermal structure with H_{400} = 1.3 km, and in which tectonomagmatic period, $P = P_M + P_T$, is varied with shown values. Length of arrows indicates long-wavelength axial topography (h), pointing down to indicate depth of axial valley. (b) Long-wavelength axial topography and (c) fault spacing versus P. Dashed line is at 280 ka, which is the age contrast between successive faults at the preferred spacing of ~7.08 km. Solid curve is the distance of spreading during one tectonomagmatic cycle (i.e., $\Delta S = PU$). Error bars show maximum and minimum fault separation within each model run.

3.2. Varying the Duration of Tectonomagmatic Cycle $P = P_M + P_T$

[20] Figure 4 illustrates the key results of varying the duration of the tectonomagmatic period P between 10.0 and 502.5 ka for $F_M = 0.8$, $\eta_m = 1 \times 10^{27}$ Pa s, and $U = 25$ km/Ma. For the lower values of P (in this case $P \leq 162.5$ ka), long-wavelength axial height, h, shows little change, varying by <0.11 km about an average of −0.64 km (Figure 4b). The spacing between adjacent faults ΔS is also insensitive to P for the shorter cycles, remaining within 0.8 km of an average of 7.08 km for $P \leq 42.5$ ka (Figure 4c). The age contrast between successive faults represented by the preferred fault spacing is 7.08 km/25 km Ma^{-1} = 280 ka. It thus appears that when P is less than this age contrast, fault behavior is controlled mechanically by the balance between the pulling force need to keep a fault active and that needed to break a new fault nearer to the axis. This force balance is detailed in Paper 1.

[21] For $P > 162.5$ ka, h becomes progressively more negative, and for $P \geq 160$ ka, ΔS increases linearly with P. For these longer cycles, fault spacing is controlled primarily by the temporal variability between tectonic and magmatic periods; i.e., faults form simultaneously on both plates, remain active for only one tectonic period, and then move away from the axis during the magmatic phase. Subsequent fault pairs form during the next tectonic period. The curve in Figure 4c is the product of P and spreading rate U and shows a good match with model fault spacing.

[22] The remainder of the paper will focus on cases in which P is small enough for fault spacing to be controlled mechanically by the force required to sustain active faults versus breaking new ones. Specifically, the tectonic period P_T is held constant at 3 ka and we vary P_M to change F_M; for F_M = 0.7–0.975, P = 10–120 ka, respectively. For F_M = 1, P_T = 0.0 ka.

3.3. Importance of F_M on Fault Spacing and Heave

[23] Figure 5a summarizes our results for varying the magmatic time fraction F_M in models with imposed thermal structure. Example topographic

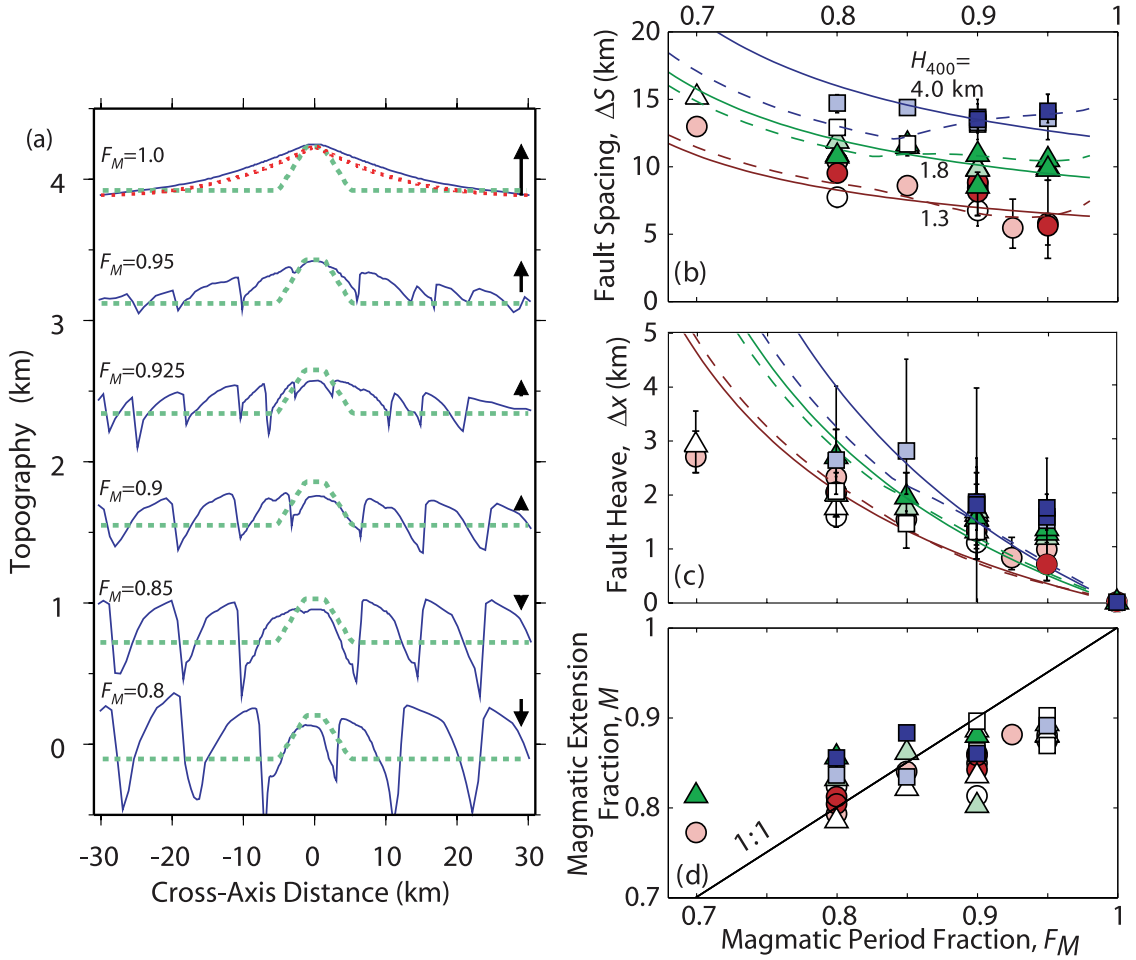

Figure 5. (a) Bathymetry profiles (solid blue) predicted for cases in which U = 25 km/Ma, $\eta_m = 5 \times 10^{18}$ Pa s, imposed thermal structure, H_{400} = 1.3 km, and varying F_M (case with F_M = 0.8 is the same as in Figures 2b–2d and Figure 3). Dashed green profiles show topography predicted for isostatic equilibrium. Dotted red profile shows topography due to thin plate flexure with accretion after *Shah and Buck* [2001]. Predicted (b) average fault spacing (c) fault heave, and (d) fraction magmatic strain M versus F_M for cases in which axial lithosphere thickness is H_{400} = 1.3 km (circles), 1.8 km (triangles), and 4.0 km (squares). The lack of systematic changes between groups of different η_M ($\eta_M = 1 \times 10^{27}$ and 1×10^{19}Pa s (white), 5×10^{18}Pa s (light colors), 2.5×10^{18} and 1.25×10^{18}Pa s (dark colors)) shows that η_M does not influence the overall trends. Solid curves are equation (1) in Figure 5b and equation (2) in Figure 5c in which x_{AF} = 3.1 km (red), 4.5 km (green), and 6.0 km (blue). Dashed colored curves show calculations with variable x_{AF} as computed by the force balance model in Paper 1, except here, the bending force, (equation (B4), Paper 1) is proportional to $\theta^{3/2}$ [*Buck*, 1993], where θ is fault dip. In our models, θ rotates from 53° to 30° as heave increases from 0 to ~2.3 km. M is computed based on the best fitting slope of cumulative fault heave versus cross-axis distance; thus the numerical model heaves lie below and above the theoretical curves in Figure 5c where $M < F_M$ and $M > F_M$, respectively, in Figure 5d.

profiles are shown for cases in which $\eta_m = 5 \times 10^{18}$ Pa s and H_{400} = 1.3 km (Figure 5a). When the ridge remains in the magmatic phase at all times (F_M = 1) a distinct axial high forms without any faults (Figure 5a). Compared to the isostatic topography (dashed green), the calculation (solid blue) predicts a total variation in topography that is slightly greater and distributed over a broader distance from the axis. Both of these differences are consistent with the topography being controlled by the flexure of accreting lithosphere [*Buck*, 2001] the key cause for the dynamic topography is the resistance of initially curved lithosphere to unbend, which transfers some of the weight of the axis to its flanks, thus depressing the flanks much like "flexural moats". The topographic profile for F_M = 1 shows good match with a separate calculation (red dotted curve) of an accreting elastic lithosphere, based on thin-plate theory [*Shah and Buck*, 2001] and using the same density structure and variation

in effectively elastic plate thickness (assumed to correspond to the depth of the 600°C isotherm).

[24] Faults form whenever $F_M < 1$. With $\eta_m = 5 \times 10^{18}$ Pa s, axial height grows rapidly during magmatic phases and approaches the isostatic height. As F_M decreases, the amount of time spent in the magmatic phase decreases, and thus the total uplift is less. Also as F_M decreases, topography away from the axis is increasingly influenced by faulting. For the case shown in Figure 5a, long-wavelength topography can be characterized as faulted axial highs when $1.0 > F_M \geq 0.925$, transitional when $0.9 \geq F_M \geq 0.85$, and beginning to approach an axial valley when $F_M = 0.8$. Thus, F_M is one parameter that influences long-wavelength topography.

[25] The major influence of F_M, however, is on the short-wavelength fault topography. Figures 5b and 5c show the results for our imposed temperature calculations with $H_{400} = 1.3$, 1.8, and 4.0 km for all values of $\eta_M = 1.25 \times 10^{18}$ to 1×10^{27} Pas. Models predict fault spacing ΔS and heave Δx to increase with decreasing F_M, in a manner that is reasonably well explained by the following scaling for fault spacing:

$$\Delta S = \frac{F_M}{(F_M - 0.5)} x_{AF}, \quad (1)$$

and heave

$$\Delta x = \frac{(1 - F_M)}{(F_M - 0.5)} x_{AF}, \quad (2)$$

where x_{AF} is the maximum distance that a fault moves away from the axis while remaining active (before a new fault forms on the opposite plate). These equations come from simple kinematic arguments formulated by *Buck et al.* [2005] and further developed in Paper 1. They have the same form as equations (3) and (4) of Paper 1 but with the temporal fraction F_M replacing the kinematic fraction M of the plate spreading rate that is accommodated magmatically. The ability to explain our model predictions with equations (1) and (2) implies that M is simply related to F_M (Figure 5d). We see no systematic deviation from these trends with η_M, which indicates that the rate of axial topographic growth during magmatic phases does not strongly influence fault characteristics.

[26] Comparisons between model predictions and equations (1) and (2) are shown in Figures 5b and 5c. Each solid curve is for a constant, representative value of x_{AF} taken from the numerical model runs for a given value of H_{400}. The force balance arguments developed in Paper 1 predict similar values of x_{AF} that vary by a small amount with F_M (dashed). Fault distance x_{AF}, and thus ΔS and Δx are all predicted to be larger for larger axial lithosphere thickness (Figures 5b and 5c). The cause can be understood in context the force balance arguments as follows. Off-axis distance x_{AF} is limited by the point at which the net tectonic pulling force $\mathcal{F}$ needed to keep the fault active exceeds the strength $\mathcal{F}_I$ of the intact lithosphere nearer to the axis (i.e., $\mathcal{F} > \mathcal{F}_I$, at which point a new fault forms and takes over). The net pulling force $\mathcal{F}$ is the sum of those needed to bend the lithosphere near the active fault $\mathcal{F}_B$ and to overcome friction and strain-weakened cohesion on the fault $\mathcal{F}_F$ (i.e., $\mathcal{F} = \mathcal{F}_B + \mathcal{F}_F$). The bending part $\mathcal{F}_B$ increases as the lithosphere thickens off axis, whereas $\mathcal{F}_F$ initially decreases due to cohesion loss with fault slip but then increases with lithosphere thickness once weakening is complete. Here x_{AF} is predicted to decrease with H_{400} if the rate of off-axis thickening is proportional to H_{400} because $(\mathcal{F}_B + \mathcal{F}_F)/\mathcal{F}_I$ increases toward 1 more rapidly with off-axis distance for larger H_{400} (Paper 1). However, in the cases considered here, the rate of off-axis thickening is not proportional to H_{400}; it is held constant. Consequently, the fractional rates that lithosphere thickness and $(\mathcal{F}_B + \mathcal{F}_F)$ increase off axis are smaller for larger H_{400}, thus allowing $(\mathcal{F}_B + \mathcal{F}_F)/\mathcal{F}_I$ to remain <1 and the fault to remain active to a greater distance x_{AF} away from the axis. This result further illustrates our findings in Paper 1.

3.4. Influence of H_{400}, η_M, and U on the Transition Between Axial Highs and Median Valleys

[27] Figure 6 shows predicted bathymetry profiles in which $U = 25$ km/Ma, $H_{400} = 1.3$ km, $F_M = 0.9$, and the maximum viscosity parameter η_M (see section 2.2) in the magma zone is varied from 1.25×10^{18} to 1×10^{27} Pa s. Again, η_M does not change fault characteristics in a systematic manner. The major influence of η_M is on the long-wavelength topography. When the maximum viscosity is not altered from the basic temperature- and stress-dependent rheology (i.e., $\eta_M = 1 \times 10^{27}$ Pa s), the growth of topography during the magmatic phases is suppressed by the strong axial lithosphere, even though the nonlithostatic stresses associated with extension are completely removed. The result is a prominent axial valley (lowermost profiles in Figure 6). As η_M is decreased to 1×10^{19} Pa s, so does the characteristic timescale

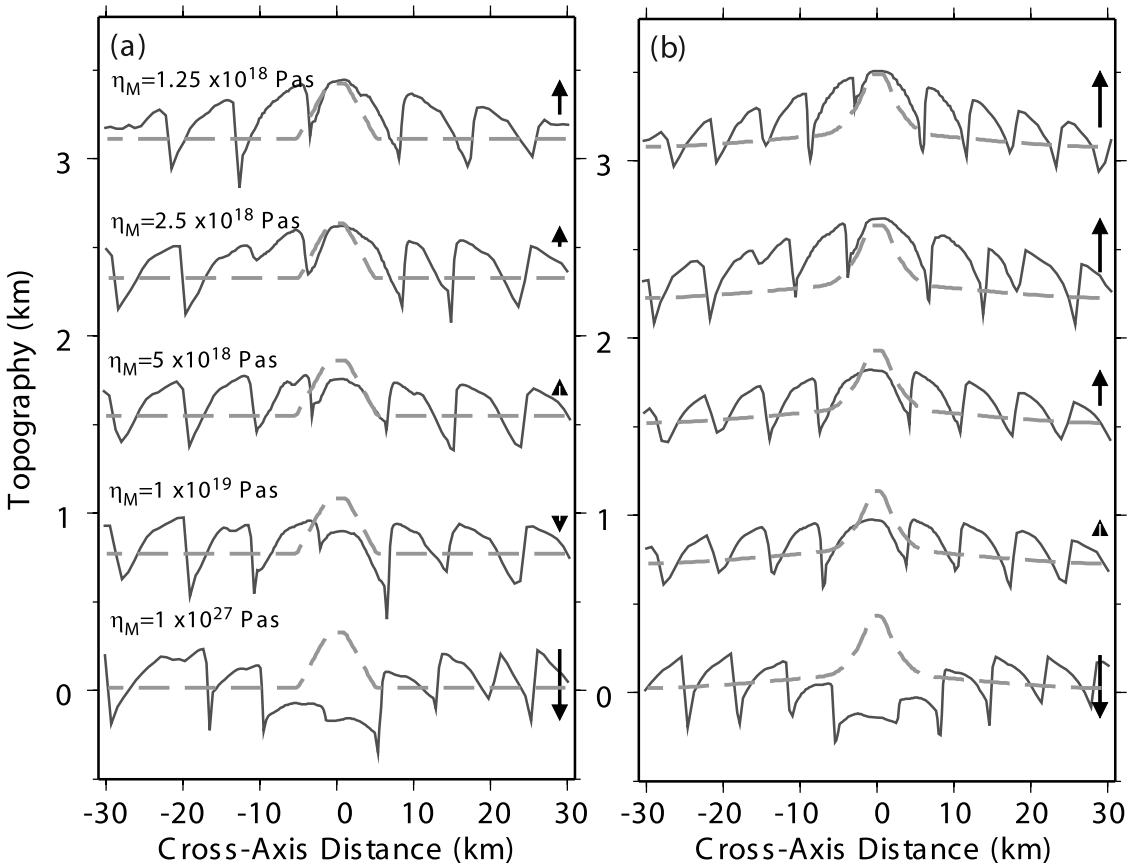

Figure 6. Predicted bathymetry profiles for cases in which $U = 25$ km/Ma, $F_M = 0.9$, $H_{400} = 1.3$ km and in which η_m is varied as shown. (a) Imposed thermal structure (lithosphere thickness is constant for $|x| > 8$ km) and (b) computed thermal structure (thickening lithosphere throughout). Dashed curves (as in Figure 5) show isostatic topography.

τ_M for topographic growth during the magmatic phases (τ_M is proportional to η_M), and the axial valley is replaced by flat, faulted topography, which often characterizes the "transitional" morphology at intermediate spreading rates (e.g., Figure 1). With further reduction of η_M below 1×10^{19} Pa s, a faulted axial high emerges. Cases with imposed (Figure 6a) and computed (Figure 6b) thermal structure predict the same gross morphology but the latter predicts slightly greater axial heights overall. The main reason for this difference is that lithosphere continues to thicken away from the axis when temperatures are computed but remains constant in the imposed thermal models (see Figures 2d and 2g).

[28] Figure 7 summarizes our findings of long-wavelength axial heights, h, for all calculations in which η_M was varied. The results reveal an exponential dependence of h on the shown function of F_M and η_M. A conceptual way of understanding these results is to consider the isostatic adjustment of topography during a single magmatic period. At the beginning of this period (time $t = 0$), axial topography is fully depressed to a depth w_T from the previous a tectonic period. Then as magmatism occurs, the height of the ridge axis relaxes toward the height of isostatic equilibrium (h_M). Assuming only viscous relaxation (as opposed to the combined effects of viscoelastic plasticity, which is simulated in models), the height of the ridge axis evolves in time according to [e.g., *Turcotte and Schubert*, 2002]

$$h = -w_T + (w_T + h_M)\left(1 - \exp\left[\frac{-t}{\tau_M}\right]\right). \quad (3)$$

The relaxation timescale τ_M depends on the density contrast between mantle and water $\Delta\rho$, gravitational acceleration g, and the wavelength of the topography λ, and on viscosity η_M, according to

$$\tau_M = \frac{4\pi\eta_M}{\Delta\rho g\lambda}. \quad (4)$$

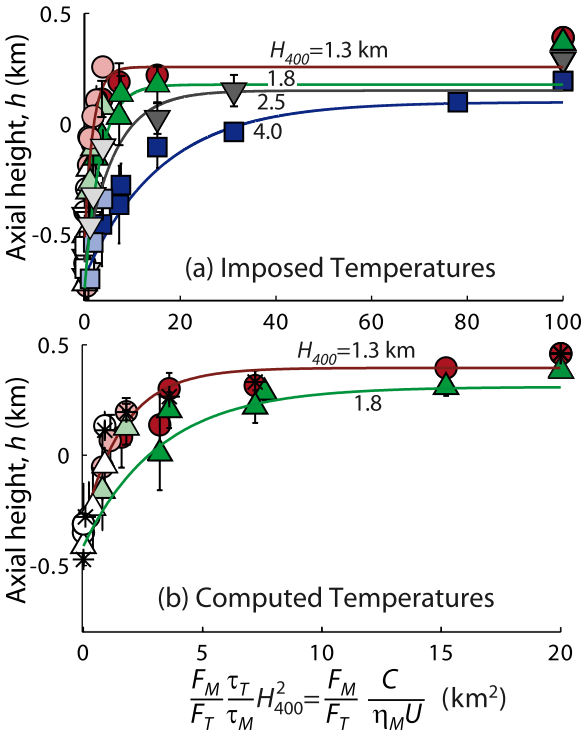

Figure 7. Predicted axial height, h, for cases in which thermal structure is (a) imposed and (b) computed and U = 25 km/Ma, each on different horizontal scales. Horizontal axis is rise-sink ratio times H_{400}^2 (equations (6) and (7)). Symbols distinguish results of calculations with different H_{400}: 1.3 km (circles), 1.8 km (up-pointing triangles), 2.5 km (down-pointing triangles), and 4.0 km (squares). Color shading denotes groupings according to viscosity: (white) $\eta_M = 1 \times 10^{27}$ and 1×10^{19}Pa s, (light) $\eta_M = 5 \times 10^{18}$Pa s, and (dark) $\eta_M = 2.5 \times 10^{18}$ and 1.25×10^{18}Pa s, except for the one square at $(F_M/F_T)(\tau_T/\tau_M)\ H_{400}^2 \sim 78$ km^2 for which $\eta_M = 5 \times 10^{17}$Pa s. Results for $F_M = 1$ are plotted at arbitrary locations on the right side of the diagram; they lie above the theoretical curves (equations (6) and (7)) as predicted by the effects of lithosphere flexure (see text). Asterisks show results for models with smaller faults (see text) shown in Figure 10 in which η_M varies from 1×10^{27} to 1.25×10^{18} Pa s, from left to right.

[29] While equation (3) describes the evolution of h during a single magmatic cycle, we find that the time-integrated results of many tectonomagmatic cycles can be explained by replacing the dimensionless time in the exponential of (3) with

$$\frac{P_M/\tau_M}{P_T/\tau_T} = \left(\frac{F_M}{F_T}\right)\left(\frac{\tau_T}{\tau_M}\right). \quad (5)$$

This is the ratio of the time fractions for topography to rise, P_M/τ_M, and sink, P_T/τ_T, where τ_T is the characteristic time for topography to sink during the tectonic phase and recalling that $F_T = 1 - F_M$. The inverse of the timescales, $1/\tau_M$ and $1/\tau_T$ are the characteristics rates that topography rises during magmatic phases and sinks during tectonic phases, respectively. Thus P_M/τ_M and P_T/τ_T represent the total (fractional) amounts that the axis can rise and sink, respectively. We therefore refer to equation (5) as the topographic "rise-sink ratio."

[30] The numerical results are well explained by a scaling law of the same form as (3),

$$h = -w_T + (w_T + h_M)\left\{1 - \exp\left[-\left(\frac{F_M}{F_T}\right)\left(\frac{\tau_T}{\tau_M}\right)\right]\right\}, \quad (6)$$

in which,

$$\left(\frac{F_M}{F_T}\right)\left(\frac{\tau_T}{\tau_M}\right) = \left(\frac{F_M}{F_T}\right)\left(\frac{C}{\eta_M H_{400}^2 U}\right), \quad (7)$$

where U is half spreading rate and C is an empirical constant, $C = 7.92 \times 10^{14}$ Nm. In Figure 7, axial height h is plotted versus $(F_M/F_T)(\tau_T/\tau_M)\ H_{400}^2$, which was varied by changing η_M in equation (7). The H_{400}^2 term is included to illustrate the differences between cases with different values of H_{400} (different symbols). Best fits to the model results are achieved when the maximum valley depth w_T is estimated as the average of axial heights for all cases with $\eta_M = 1 \times 10^{27}$ Pa s, and

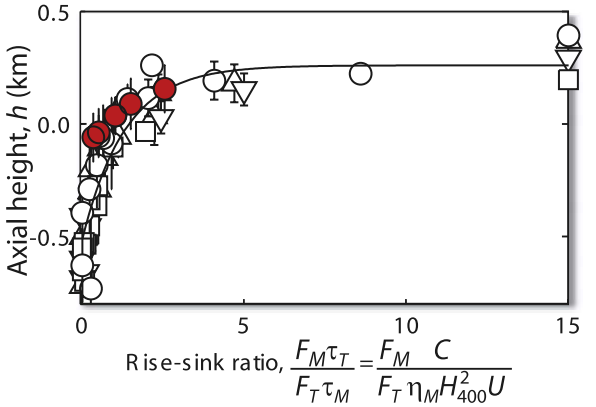

Figure 8. Red circles shows predicted long-wavelength topography for different spreading rates, U. From left to right, U = 75, 50, 25, 17, 10 and km/Ma, thus illustrating the predicted increase in rise-sink ratio with decreasing spreading rate. Changing rise-sink ratio by changing U is indistinguishable from changing rise-sink ratio by changing η_M, F_M, and H_{400} as illustrated by comparing with all cases with U = 2.5 km/Ma shown in Figure 7. Symbols denote differences in H_{400} as in Figure 7. Curve is full scaling law, equations (6) and (7) for H_{400} = 1.3 km. Case with $F_M = 1$ is on far right of plot.

shallowest axial high topography h_M as the height of the calculation with the largest rise-sink ratio $(F_M/F_T)(\tau_T/\tau_M)$ for $F_M < 1$. All cases with $F_M = 1$ predict $h > h_M$ due to the effects of flexure to produce a total relief that exceeds the isostatic topography (Figure 5 and *Buck* [2001]). Figure 8 shows results of all cases with imposed thermal structure plotted versus rise-sink ratio. They closely follow the theoretical curve for H_{400} = 1.3 km; some of the scatter is due to differences in maximum and minimum height, h_M and w_T, respectively.

[31] The form of (7) is mostly intuitive. First, the proportionality between τ_M and η_M in equation (4) accounts for η_M being in the denominator of (7). Second, the inverse dependence of rise-sink ratio on H_{400}^2 probably reflects the fact that increasing H_{400} decreases the vertical pressure gradient that drives upwelling by both increasing the thickness of the lithosphere channel through which the low-viscosity material rises and by decreasing the non-lithostatic pressure below this channel due to partial melt in the crust. Decreasing melt pressure with lithosphere thickness also reduces axial topography for $(F_M/F_T)(\tau_T/\tau_M) = \infty$ (i.e., $F_M = 1$) as evident in Figures 7 and 8. Last, the proportionality between the characteristic sinking rate $1/\tau_T$ and half spreading, U can be predicted because, in our models, extension-driven faulting is the main process that depresses the ridge axis [see also *Qin and Buck*, 2005]. This dependence is revealed by comparing the results of cases with different U. Figure 8 shows that when the rise sink-ratio is varied by changing U between 10 and 75 km/Ma, the heights h lie along the same trend as the results presented in Figure 7a, also following the exponential curve given by (6).

4. Discussion

4.1. Geologic Meaning of *P*

[32] The tectonomagmatic cycle, P, simulated in our numerical experiments involves times when extension is accommodated entirely magmatically (M = 1) and entirely amagmatically (M = 0). We therefore envision P to represent natural time spans less than the $\sim 10^3$ ka episodicity inferred from variations in axial topography [*Pockalny et al.*, 1988] or gravity [*Tucholke and Lin*, 1994], which probably represent longer period fluctuations in magma flux. P is likely to be more comparable to the age contrast between individual eruptive units, i.e., 10^{-3}–10^{1} ka [*Curewitz and Karson*, 1998; *Perfit and Chadwick*, 1998; *Sinton et al.*, 2002]. If, in extreme cases, the full tectonomagmatic time period is large enough to control the spacing of faults (see Figure 4c), as has been suggested for the Juan de Fuca Ridge [*Kappel and Ryan*, 1986], then it would be $\sim 10^2$ ka [*Canales et al.*, 2005].

4.2. Importance of F_M

[33] The importance of the magmatic time fraction F_M on faulting and axial height can be examined with observations. From bathymetry profiles across different mid-ocean ridges, we have estimated fault characteristics, axial height, and the kinematic fraction M of tectonic extension (see Figure 9 caption and Paper 1 and Table 2). If we assume F_M equals M, we can compare observations with our predictions. First, we see that the observed fault spacing ΔS increases with decreasing M as predicted by equation (1) (Figure 9a). Nearly the full range of observations is encompassed by the theoretical curves with x_{AF} ranging 0.5–1.7 km.

[34] Figure 9b compares observed axial height (h, computed in the same way as the model topography) versus M with predictions of equation (6), except with the rise-sink ratio in the exponent described as $M/(1\text{-}M)(\tau_T/\tau_M)$. Indeed the observations show decreasing axial height with decreasing M consistent with the predicted decrease in h with F_M. The above consistencies between observations and predictions supports (6) and our assumption that $F_M \sim M$. Our study therefore predicts that F_M controls both fault characteristics and axial height and does so for distinct reasons: F_M controls faulting through its relation with the kinematics of extension (i.e., M) [*Buck et al.*, 2005; Paper 1], and influences axial height through its control on the relative time for building versus reducing topography $F_M/(1 - F_M)$ $(=F_M/F_T)$.

4.3. Importance and Geologic Meaning of τ_T/τ_M

[35] The positive relationship between F_M and h that is predicted by equation (6) is also exhibited by the data, however, the full range of axial heights can only be explained if τ_T/τ_M changes from relatively high values ($\sim$0.6) for the tallest axial highs at the Juan de Fuca and Galapagos spreading centers to lower values ($\sim$0.01) for the deepest valleys along the Mid-Atlantic Ridge (Figure 9b). The inverse relationship between τ_T and spreading rate is opposite the global tendency for axial valleys (low τ_T/τ_M) to occur at slow spreading

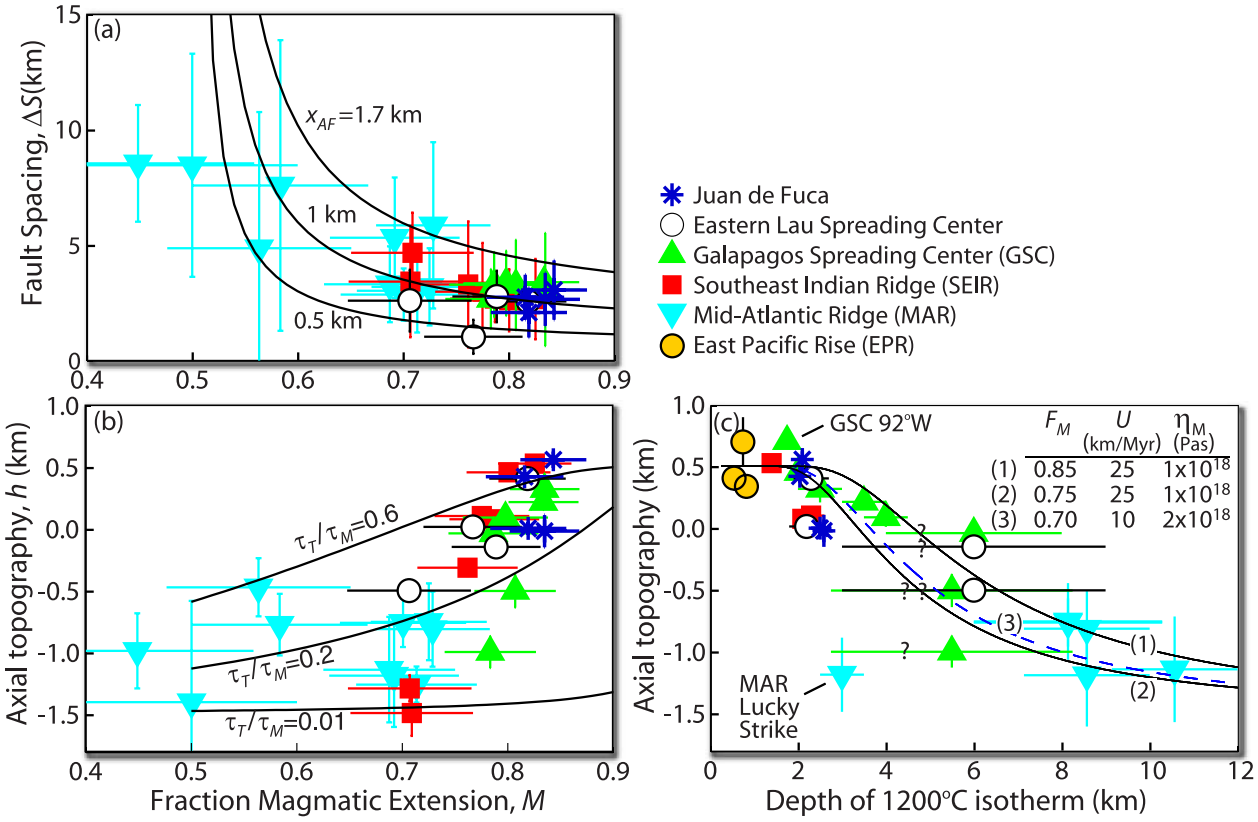

Figure 9. Observed (a) fault spacing ΔS and (b) axial height h versus fraction magmatic extension M (symbols for different ridges labeled; data given in Table 2). Curves in Figure 9a are equation (1) with M replacing F_M, assuming different distances that faults remain active x_{AF}. Curves in Figure 9b are equation (6) with M replacing F_M, w_T = 1.5 km and h_M = 0.5 km, and different ratios of timescales for topographic reduction versus growth τ_T/τ_M. (c) Axial height versus depth of 1200°C isotherm beneath the axis, which is assumed to be the depth (with published uncertainties) of seismically imaged magma lenses for all points with depths <5.0 km (EPR [*Tolstoy et al.*, 1997; *Carbotte et al.*, 1998], GSC [*Blacic et al.*, 2004], SEIR [*Baran et al.*, 2005], Lau Basin [*Jacobs et al.*, 2007], Juan de Fuca [*Canales et al.*, 2005], MAR, Lucky Strike [*Singh et al.*, 2006]). Symbols with question marks indicate points where the magma lens was not imaged and therefore 1200°C is arbitrarily assumed to be at the base of the crust. For the MAR points at depths >8.0 km, depths are given as depths of the deepest earthquakes near 28.95°–29.19°N (*Wolfe et al.* [1995] and estimated uncertainties) multiplied by a factor of 1.4, which is based on the assumption that the deepest earthquakes occur at 600°C and that the geothermal profiles are the same as in our models. Theoretical curves assume 1200°C occurs at a depth of $2.5H_{400}$ (again to be consistent with model geotherms). Published figures are used to estimate axial height h for the EPR [*Weiland and Macdonald*, 1996; *Tolstoy et al.*, 1997] and Lucky Strike [*Cannat et al.*, 1999]. Curves are equations (6) and (7) with shown parameter values. The GSC and MAR estimates are matched by the solid and dashed curves respectively.

rates and highs (high τ_T/τ_M) at fast rates. The most logical explanation is therefore that there is a corresponding global tendency for τ_M to decrease more rapidly than τ_T with spreading rate. Also, the relatively good correlation between h with M seen in data for $M \geq \sim 0.7$ is much steeper than the trend predicted by (6) for any single value of τ_T/τ_M. We can thus interpret this discrepancy as indicating that τ_T/τ_M and F_M ($\sim M$) often change together in nature.

[36] One possible explanation for this correlation has to do with the predicted influence of lithosphere thickness on τ_T/τ_M in equation (7). Figure 9c shows estimates of axial topography at various ridges versus the depth to the 400°C isotherm, which is based the depths of earthquakes (MAR other than Lucky Strike) and seismically imaged magma lenses. The observations show a dominant trend of decreasing axial height with increasing H_{400}, which is well explained by equations (6) and (7). A simple explanation for τ_T/τ_M varying naturally with F_M (and M) is that, if F_M is closely related to magma flux, then changes in magma flux and F_M lead to changes in lithosphere thickness as

Table 2. Ridge-Perpendicular Bathymetry Profiles Used in Our Analysis Cross the Ridges at the Shown Locations[a]

On-Axis Location of Ridge-Perpendicular Transect (Lat. °N, Lon. °E)	Nontectonic Strain M	Mean Fault Spacing ΔS (km)	Long-Wavelength Axial Height h (km)
	Mid-Atlantic Ridge (MAR)		
28.95, −43.22	0.73 ± 0.05	5.8 ± 3.6	−0.82 ± 0.30
29.00, −43.21	0.69 ± 0.06	5.3 ± 2.6	−1.19 ± 0.42
29.05, −43.20	0.69 ± 0.06	3.3 ± 1.6	−1.15 ± 0.43
29.11, −43.18	0.71 ± 0.05	3.0 ± 1.8	−1.27 ± 0.15
29.15, −43.17	0.70 ± 0.06	2.9 ± 1.1	−0.77 ± 0.19
29.19, −43.15	0.73 ± 0.05	3.2 ± 1.7	−0.76 ± 0.31
26.72, −44.55	0.58 ± 0.08	7.6 ± 6.3	−0.78 ± 0.25
26.66, −44.57	0.56 ± 0.08	4.9 ± 5.9	−0.48 ± 0.23
23.37, −44.91	0.45 ± 0.11	8.5 ± 2.5	−0.99 ± 0.30
23.45, −44.91	0.50 ± 0.10	8.5 ± 4.8	−1.41 ± 0.82
	Southeast Indian Ridge (SEIR)		
−47.38, 100.75	0.83 ± 0.03	2.6 ± 1.7	0.52 ± 0.04
−47.45, 100.95	0.80 ± 0.04	2.6 ± 1.3	0.45 ± 0.05
−47.73, 101.75	0.79 ± 0.04	2.7 ± 1.0	0.07 ± 0.05
−47.95, 103.52	0.78 ± 0.05	3.0 ± 2.1	0.10 ± 0.05
−49.65, 109.85	0.76 ± 0.04	3.3 ± 2.7	−0.32 ± 0.07
−49.97, 115.00	0.71 ± 0.06	3.4 ± 2.4	−1.30 ± 0.11
−49.87, 114.50	0.71 ± 0.06	4.7 ± 1.7	−1.50 ± 0.18
	Galapagos Spreading Center (GSC)		
2.14, −96.99	0.78 ± 0.04	2.7 ± 1.3	−1.00 ± 0.13
2.30, −96.02	0.81 ± 0.04	3.3 ± 2.0	−0.51 ± 0.13
2.59, −94.70	0.79 ± 0.04	3.3 ± 1.4	−0.04 ± 0.06
2.53, −94.24	0.80 ± 0.04	3.3 ± 1.4	0.08 ± 0.08
2.48, −93.71	0.83 ± 0.03	3.4 ± 0.6	0.21 ± 0.06
2.28, −92.98	0.84 ± 0.03	3.1 ± 2.5	0.31 ± 0.11
	Eastern Lau Spreading Center		
−21.61, 183.58	0.82 ± 0.03	2.5 ± 0.2	0.40 ± 0.09
−21.19, 183.69	0.77 ± 0.05	1.0 ± 0.7	0.01 ± 0.04
−20.36, 183.86	0.71 ± 0.06	2.6 ± 1.3	−0.51 ± 0.06
−19.85, 0183.95	0.79 ± 0.04	2.8 ± 1.1	−0.15 ± 0.04
	Juan de Fuca		
44.70, −130.34	0.82 ± 0.04	2.7 ± 1.0	0.42 ± 0.05
44.82, −130.29	0.84 ± 0.03	3.0 ± 1.3	0.55 ± 0.07
45.30, −130.08	0.83 ± 0.03	2.6 ± 1.2	−0.03 ± 0.13
45.39, −130.03	0.82 ± 0.04	2.1 ± 1.1	−0.00 ± 0.05

[a] Fault tops and bottoms were picked based on along-axis continuity of bathymetric lineaments (examples given in Figure 1), assuming all faults are inward facing. M is estimated from the best fitting slope of cumulative fault heave versus distance on both sides of the axis; errors estimated to be ±20% the slope. Faults spacing is the mean distance between adjacent fault bases with errors being one standard deviation. Values of ΔS are consistent with characteristic widths of abyssal hills near the flanks of the MAR and SEIR as measured by *Goff et al.* [1997]. For the MAR near 29°N, our averages of ΔS and tectonic strain (1-M) are 2–3 times larger than those of *Escartín et al.* [1999]. *Escartín et al.*'s [1999] high-resolution side-scan sonar data enabled them to identify more, smaller faults than we did, which led to their smaller spacing estimates. They also determined heave based only exposed (high backscatter) faults surfaces, whereas we have assumed the full length of the steepest slopes are part of the fault surface, whether overlain (by sediment, talus, lava) or exposed. We therefore anticipate actual fault heaves being between our and *Escartín et al.*'s [1999] estimates. Long-wavelength topography is computed the same way as we did for model predictions (see section 2.4); errors in h are the difference in heights of the faults on either side of the axis that define h. See also Paper 1 for more details.

predicted by models of crustal accretion and cooling by *Phipps Morgan and Chen* [1993a, 1993b].

[37] Other factors that could contribute to the above relation are more directly related to magma transport and primarily influence $1/\tau_M$. For example, topography can grow internally by crustal deformation associated with repeated intrusions of magma or externally by eruptions themselves. Longer magmatic periods (i.e., larger F_M) could be associated with more frequent events and higher $1/\tau_M$. Evidence for a positive correlation between eruption frequency and spreading rate (and thus with axial topography) has been presented in the

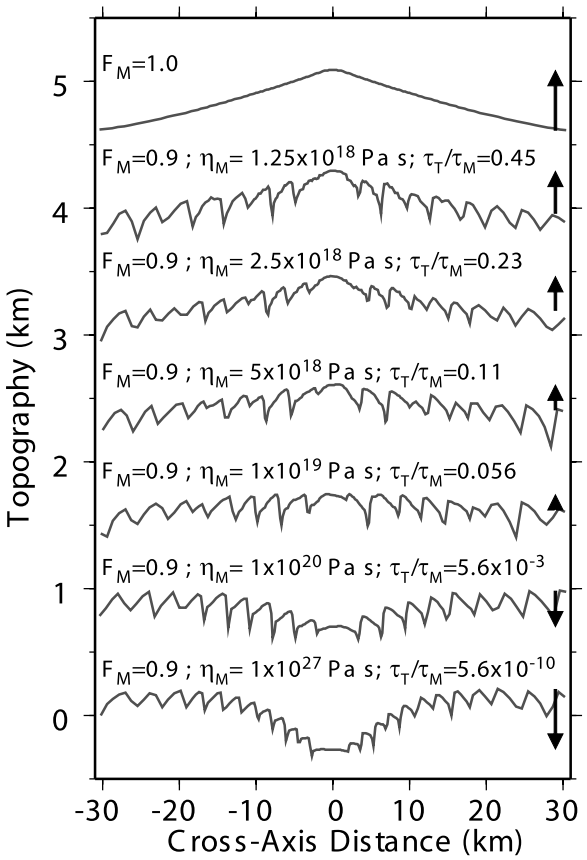

Figure 10. Predicted bathymetry profiles for cases with H_{400} = 1.3 km, U = 25 km/Ma, computed thermal structure, and shown values of F_M and η_m. Here, the minimum cohesive strength of the fault is increase to 11 MPa from 2 MPa in the prior calculations. The smaller the contrast with the unfaulted lithosphere (44 MPa) results in smaller fault spacing that is comparable to that seen on the GSC and SEIR. The depth of the 1000°C isotherm of 3.55 is comparable to the depths of magma lens reflectors seen in the regions of transitional morphology at the Galapagos Spreading Center [*Blacic et al.*, 2004], Juan de Fuca Ridge [*Canales et al.*, 2005; *Carbotte et al.*, 2006], and in the axial valley of the Lucky Strike region of the Mid-Atlantic Ridge [*Singh et al.*, 2006]. The model depth is greater than the depths of 1.5–2.1 km of the magma reflector beneath the Southeast Indian Ridge [*Baran et al.*, 2005].

literature [*Curewitz and Karson*, 1998; *Perfit and Chadwick*, 1998; *Sinton et al.*, 2002] and includes findings of sparse magmatic rocks in areas with deep axial valleys [e.g., *Cannat*, 1993, 1996; *Blackman et al.*, 2002; *Dick and Schouten*, 2003; *Michael et al.*, 2003]. The spatial pervasiveness of eruptions may also influence $1/\tau_M$ as suggested by observations of expansive sheet flows at ridges with topographic highs (high $1/\tau_M$) versus more confined pillow flows and point-source eruptions at axial-valley-dominated ridges (low $1/\tau_M$) [*Smith and Cann*, 1990; *Lawson et al.*, 1996; *Perfit and Chadwick*, 1998; *Sinton et al.*, 2002; *Behn et al.*, 2004]. Ultimately, the behavior of τ_T/τ_M in conditions of different F_M, thermal structure, and magma supply is governed by the physics of melt storage, intrusions, and eruptions.

[38] As a further illustration of the distinct effects of τ_T/τ_M and F_M in controlling axial height, we show a set of calculations designed to be more realistic in that fault spacing is more similar to those of Galapagos Spreading Center (GSC) and the South East Indian Ridge (SEIR) than our prior calculations (by imposing a slightly larger minimum cohesion of 11 MPa) (Figure 10). Thermal structure is computed, U = 25 km/Ma, and H_{400} = 1.3 km. The first case is for F_M = 1, and the other cases have F_M = 0.9 with τ_T/τ_M changing between 0.45 and 10^{-10} by varying η_M between 1.25×10^{18} Pa s and 1×10^{27} Pa s. First, even though fault spacing and heave are much smaller than in the previous calculations, the long-wavelength topography closely matches those shown in Figure 7b, with the same parameters. This result illustrates the robustness of our method of separating long- and short-wavelength topography. Second, changing τ_T/τ_M alone yields the full range of axial morphologies observed along the GSC and SEIR. Last, Figure 10 further illustrates that the rise-sink ratio (F_M/F_T) (τ_M/τ_T) is the primary quantity that controls the transition in ridge-axis morphology from axial topographic highs, to intermediate morphology lacking a high or valley, to deep median valleys.

4.4. Variations in Axial Morphology That Deviate From Global Trends

[39] A key prediction we make is that magma supply and axial thermal structure correlate with or control topography to the extent that they correlate with or control the rise-sink ratio $(F_M/F_T)(\tau_T/\tau_M)$. At odds with the mechanical influence proposed by Chen and colleagues [e.g., *Phipps Morgan and Chen*, 1993a, 1993b; *Chen and Morgan*, 1990a, 1990b], Figure 10 as well as previous studies [*Buck et al.*, 2005; *Qin and Buck*, 2005; Paper 1] show that rift valley-like morphology can occur independent of the amount of mechanical coupling between the crustal lithosphere and mantle peridotite and often beneath moderately thin lithosphere. Figure 9c shows good evidence for lithosphere thickness being a prominent factor but it also illustrates the importance of

other factors that influence the rise-sink ratio. For example, explaining the axial topography of the MAR near 29°N with $F_M \sim 0.7$ (Figure 9b, 9c) requires a factor of two larger η_M than needed to explain the topographic trend of the GSC (green, Figure 9c).

[40] The Lucky Strike area, where *Singh et al.* [2006] image a magma lens beneath an axial valley, is a clear outlier to overall trend of the other observations. One explanation is a higher η_M, which again is likely to reflect distinct physical processes of magma storage, intrusions, and eruptions. That is, magma supply is sufficient to sustain a hot crust but η_M is too high, and $(F_M/F_T)(\tau_T/\tau_M)$ is too low to fill in the axial valley at present day. Another explanation is that the Mid-Atlantic Ridge is an example where along-axis variations in structure are large [*Lin and Phipps Morgan*, 1992; *Escartín and Lin*, 1995; *Escartín et al.*, 1999] and therefore where the morphology at any given location can be influenced heavily by structure or processes at other locations along-axis. This possibility would suggest that the effective values of H_{400}, η_M, or both are greater than the local values above the Lucky Strike magma lens. Ultimately, full 3-D calculations are need to more completely understanding how local topography responds to along-axis variations in the rise-sink ratio.

[41] The Juan de Fuca Ridge is another example of where the axial morphology does not follow a simple relationship with lithosphere thickness. *Carbotte et al.* [2006] emphasized that the height of a small but prominent axial graben seen on the ridge does not correlate positively with axial magma lens depth as is usually expected. Instead, in three to four of the five segments considered, the magma lens tends to shoal as graben height increases. Following *Chadwick and Embley* [1998], *Carbotte et al.* [2006] proposed that these axial grabens are driven not by seafloor spreading but instead by tension occurring above near-vertically intruding dikes. A seafloor spreading origin, however, is still possible if $(F_M/F_T)(\tau_T/\tau_M)$, and thus surface faulting, are sufficiently decoupled in time from lithosphere thickness (i.e., magma lens depth). Different spatial and timescales of magma storage, transport, and eruptions, (i.e., η_M) can cause such decoupling. Another point to consider is that if the duration of the tectonomagmatic cycle P is long enough to control fault spacing [*Kappel and Ryan*, 1986; *Canales et al.*, 2005] (i.e., P is longer than age contrast of the mechanically preferred fault spacing, Figure 4), then the deepest graben would correspond to both maximum (end of tectonic period) and minimum (end of magmatic period prior to new faults forming) lithosphere thicknesses.

[42] Last, the Lau Spreading Center displays a clear exception to the overall tendency for a positive correlation between axial height and spreading rate [*Martinez et al.*, 2006]. Here, axial topography decreases from a prominent high in the south (Valu Fa Ridge) to a faulted axial valley in the northern section of the Eastern Lau Spreading Center (ELSC) in the face of both a doubling in spreading rate (and magma supply) as well as a northward shoaling of the axial magma lens between Valu Fa and the central ELSC [*Jacobs et al.*, 2007]. This is clearly opposite to global trends as emphasized by *Martinez et al.* [2006]. However, this trend is, in fact, consistent with our prediction that $\tau_T/\tau_M \sim 1/U$. The ELSC could be unusual from most other ridges in that the $1/U$-dependence is accentuated by the large change in spreading rate (39–97 km/Ma) over a relatively short distance, thus being the dominant factor in the northward reduction of the rise-sink ratio.

5. Conclusions

[43] Our numerical models simulate the time-dependent behavior of alternating magmatic and tectonic cycles at mid-ocean ridges to investigate the origin the different morphologies seen throughout the global ridge system. We find that if the duration of the full tectonomagmatic cycle P is comparable to or greater than the seafloor age contrast represented by the mechanically preferred fault spacing, faults form and growth only during subsequent tectonic phases and thus fault spacing and size increase linearly with P. When P is less than the age contrast of the preferred spacing, as is the case for the remaining results, the overall faulting pattern and long-wavelength morphology are independent of P. The mechanically preferred spacing is controlled by the net force required to keep an active fault slipping as it moves off-axis and the force needed to create a new fault by breaking the lithosphere near the axis.

[44] One key parameter that influences axial morphology is the time fraction spent in the magmatic phase F_M. Observations support our predictions that fault spacing and total heave are sensitive to F_M, both increasing with decreasing F_M in much the same way as simple theory predicts spacing and heave to change with kinematic fraction M of

magmatic extension [*Buck et al.*, 2005; Paper 1]. The key parameter that controls the global transition between axial topographic highs and median valleys is the "rise-sink ratio" $(F_M/F_T)(\tau_T/\tau_M)$. A positive relation between axial height and rise-sink ratio reveals that axial height grows with larger times spent in a magmatic phase F_M relative to a tectonic phase $F_T = (1 - F_M)$, and by a larger topographic rise rate during magmatic phases compared to the sinking rate during tectonic phases τ_T/τ_M. Models predict deep axial valleys when $(F_M/F_T)(\tau_T/\tau_M) < 1$, tall axial highs when $(F_M/F_T)(\tau_T/\tau_M) \gg 1$, and faulted transitional morphology lacking a high or valley at $(F_M/F_T)(\tau_T/\tau_M) \sim 1$.

[45] A global inverse correlation between long-wavelength axial height and lithosphere thickness is explained by our new scaling laws that predict the rise-sink ratio $(F_M/F_T)(\tau_T/\tau_M)$ to decrease with lithosphere thickness. Variations along the Galapagos Spreading Center are particularly well explained by this relation. Changes in axial morphology along the Lau Spreading Center, however, show a locally opposite correlation with lithosphere thickness (within the region that the magma lens was imaged) but are consistent with our predictions that $(F_M/F_T)(\tau_T/\tau_M)$ is inversely proportional to spreading rate. Other processes more directly related to the frequency or spatial pervasiveness of magmatism also influence the rise sink ratio as evident at ridges such as the Mid-Atlantic and Juan de Fuca ridges. Understanding such processes requires a fuller understanding of the physics of magma storage and transport within or near the crust at mid-ocean ridges.

Acknowledgments

[46] Funding for this research was provided by NSF grants OCE-0327018 (MDB), OCE-0548672 (MDB), OCE-0327051 (GI), and OCE-0351234 (GI). R. Buck and J. Sinton contributed both inspiration and knowledge that improved this manuscript. We thank R. Buck, L. Lavier, and A. Poliakov for their foundational work in developing the numerical codes and making them available to us for this study. L. Lavier and an anonymous referee provided helpful reviews that led to important improvements of this manuscript. Several figures in this manuscript were produced with GMT [*Wessel and Smith*, 1995].

References

Baran, J. M., S. M. Carbotte, and J. R. Cochran (2005), Variations in upper crustal structure due to variable mantle temperature along the Southeast Indian Ridge, *Geochem. Geophys. Geosyst.*, *6*, Q11002, doi:10.1029/2005GC000943.

Barclay, A. H., D. R. Toomey, and S. C. Solomon (2001), Microearthquake characteristics and crustal Vp/Vs structure at the Mid-Atlantic Ridge, 35°N, *J. Geophys. Res.*, *106*, 2017–2034, doi:10.1029/2000JB900371.

Behn, M. D., and G. Ito (2008), Magmatic and tectonic extension at mid-ocean ridges: 1. Controls on fault characteristic, *Geochem. Geophys. Geosyst.*, *9*, Q08010, doi:10.1029/2008GC001965.

Behn, M. D., J. M. Sinton, and R. S. Detrick (2004), Effect of the Galápagos hotspot on seafloor volcanism along the Galápagos Spreading Center (90.9–97.6°W), *Earth Planet. Sci. Lett.*, *217*, 331–347, doi:10.1016/S0012-821X(03)00611-3.

Behn, M. D., W. R. Buck, and I. S. Sacks (2006), Topographic controls on dike injection in volcanic rift zones, *Earth Planet. Sci. Lett.*, *246*, 188–196, doi:10.1016/j.epsl.2006.04.005.

Blacic, T. M., G. Ito, J. P. Canales, R. Detrick, and J. Sinton (2004), Constructing the crust of the Galapagos Spreading Center 91.3°–95.5°W: Correlation of seismic layer 2A with axial magma lens and topographic characteristics, *J. Geophys. Res.*, *109*, B10310, doi:10.1029/2004JB003066.

Blackman, D. K., et al. (2002), Geology of the Atlantis Massif (Mid-Atlantic Ridge, 30 degrees N): Implications for the evolution of an ultramafic oceanic core complex, *Mar. Geophys. Res.*, *23*, 443–469, doi:10.1023/B:MARI.0000018232.14085.75.

Buck, W. R. (1993), Effect of lithospheric thickness on the formation of high- and low-angle normal faults, *Geology*, *21*, 933–936, doi:10.1130/0091-7613(1993)021<0933:EOLTOT>2.3.CO;2.

Buck, W. R. (2001), Accretional curvature of lithosphere at magmatic spreading centers and flexural support of axial highs, *J. Geophys. Res.*, *106*, 3953–3960, doi:10.1029/2000JB900360.

Buck, W. R., L. L. Lavier, and A. N. B. Poliakov (2005), Modes of faulting at mid-ocean ridges, *Nature*, *434*, 719–723, doi:10.1038/nature03358.

Canales, J. P., R. S. Detrick, S. M. Carbotte, G. M. Ken, J. B. Diebold, A. Harding, J. Babcock, M. R. Nedimovic, and E. van Ark (2005), Upper crustal structure and axial topography at intermediate spreading ridges: Seismic constraints from the southern Juan de Fuca Ridge, *J. Geophys. Res.*, *110*, B12104, doi:10.1029/2005JB003630.

Canales, J. P., R. A. Dunn, G. Ito, R. S. Detrick, and J. M. Sinton (2006), Investigating the role of magma supply on crustal accretion processes; seismic structure and axial morphology of the western Galapagos spreading center, *Eos Trans. AGU*, *87*(52), Fall Meet. Suppl., Abstract V14A-04.

Cannat, M. (1993), Emplacement of mantle rocks in the seafloor at mid-ocean ridges, *J. Geophys. Res.*, *98*, 4163–4172, doi:10.1029/92JB02221.

Cannat, M. (1996), How thick is the magmatic crust at slow spreading oceanic ridges?, *J. Geophys. Res.*, *101*, 2847–2857, doi:10.1029/95JB03116.

Cannat, M., et al. (1999), Mid-Atlantic Ridge-Azores hotspot interactions: Along-axis migration of a hotspot-derived event of enhanced magmatism 10 to 4 Ma ago, *Earth Planet. Sci. Lett.*, *173*, 257–269, doi:10.1016/S0012-821X(99)00234-4.

Carbotte, S. M., and K. C. Macdonald (1994), Comparison of seafloor tectonic fabric at intermediate, fast, and superfast spreading ridges: Influence of spreading rate, plate motions, and ridge segmentation on fault pattern, *J. Geophys. Res.*, *99*, 13,609–13,631, doi:10.1029/93JB02971.

Carbotte, S. M., R. S. Detrick, A. Harding, J. P. Canales, J. Babcock, G. Kent, E. Van Ark, M. Nedimovic, and J. Diebold (2006), Rift topography linked to magmatism at the intermediate spreading Juan de Fuca Ridge, *Geology*, *34*, 209–212, doi:10.1130/G21969.1.

Carbotte, S., C. Mutter, J. Mutter, and G. Ponce-Correa (1998), Influence of magma supply and spreading rate on crustal magma bodies and emplacement of the extrusive layer: Insights from the East Pacific Rise at lat 16°N, *Geology*, *26*, 455–458, doi:10.1130/0091-7613(1998)026<0455:IOMSAS>2.3.CO;2.

Chadwick, W. W., Jr., and R. W. Embley (1998), Graben formation associated with recent dike intrusions and volcanic eruptions on the mid-ocean ridge, *J. Geophys. Res.*, *103*, 9807–9825, doi:10.1029/97JB02485.

Chen, Y. J., and J. Lin (2004), High sensitivity of ocean ridge thermal structure to changes in magma supply: The Galapagos Spreading Center, *Earth Planet. Sci. Lett.*, *221*, 263–273, doi:10.1016/S0012-821X(04)00099-8.

Chen, Y., and W. J. Morgan (1990a), A nonlinear rheology model for mid-ocean ridge axis topography, *J. Geophys. Res.*, *95*, 17,583–17,604, doi:10.1029/JB095iB11p17583.

Chen, Y., and W. J. Morgan (1990b), Rift valley/no rift valley transition at mid-ocean ridges, *J. Geophys. Res.*, *95*, 17,571–17,581, doi:10.1029/JB095iB11p17571.

Chen, Y. J., and J. Phipps Morgan (1996), The effects of spreading rate, the magma budget, and the geometry of magma emplacement on the axial heat flux at mid-ocean ridges, *J. Geophys. Res.*, *101*, 11,475–11,482, doi:10.1029/96JB00330.

Cochran, J. R., J.-C. Sempére, and S. S. Team (1997), The Southeast Indian Ridge between 88°E and 118°E: Gravity anomalies and crustal accretion at intermediate spreading rates, *J. Geophys. Res.*, *102*, 15,463–15,488, doi:10.1029/97JB00511.

Crawford, W. C., and S. C. Webb (2002), Variations in the distribution of magma in the lower crust and at the Moho beneath the East Pacific Rise at 9°–10°N, *Earth Planet. Sci. Lett.*, *203*, 117–130, doi:10.1016/S0012-821X(02)00831-2.

Curewitz, D., and J. A. Karson (1998), Geological consequences of dike interusions at mid-ocean ridge spreading centers, in *Faulting and Magmatism at Mid-Ocean Ridges*, *Geophys. Monogr. Ser.*, vol. 106, edited by W. R. Buch et al., pp. 117–136, AGU, Washington D. C.

Detrick, R. S., P. Buhl, E. Vera, J. Mutter, J. Orcutt, J. Madsen, and T. Brocher (1987), Multi-channel seismic imaging of a crustal magma chamber along the East Pacific Rise, *Nature*, *326*, 35–41, doi:10.1038/326035a0.

Dick, H. J. B., and H. Schouten (2003), An ultraslow-spreading class of ocean ridge, *Nature*, *426*, 405–412, doi:10.1038/nature02128.

Dunn, R. A., D. R. Toomey, and S. C. Solomon (2000), Three-dimensional seismic structure and physical properties of the crust and shallow mantle beneath the East Pacific Rise at 9°30′N, *J. Geophys. Res.*, *105*, 23,537–23,555, doi:10.1029/2000JB900210.

Dunn, R. A., V. Lekic, R. S. Detrick, and D. R. Toomey (2005), Three-dimensional seismic structure of the Mid-Atlantic Ridge (35°N): Evidence for focused melt supply and lower crustal dike injection, *J. Geophys. Res.*, *110*, B09101, doi:10.1029/2004JB003473.

Escartín, J., and J. Lin (1995), Ridge offsets, normal faulting, and gravity anomalies of slow spreading ridges, *J. Geophys. Res.*, *100*, 6163–6177, doi:10.1029/94JB03267.

Escartín, J., P. A. Cowie, R. C. Searle, S. Allerton, N. C. Mitchell, C. J. MacLeod, and A. P. Slootweg (1999), Quantifying tectonic strain and magmatic accretion at slow spreading ridge segment, Mid-Atlantic Ridge, 29°N, *J. Geophys. Res.*, *104*, 10,421–10,437, doi:10.1029/1998JB900097.

Goff, J. A., Y. Ma, A. Shah, J. R. Cochran, and J.-C. Sempéré (1997), Stochastic analysis of seafloor morphology on the flank of the Southeast Indian Ridge: The influence of ridge morphology on the formation of abyssal hills, *J. Geophys. Res.*, *102*, 15,521–15,534, doi:10.1029/97JB00781.

Jacobs, A. M., A. J. Harding, and G. M. Kent (2007), Axial crustal structure of the Lau back-arc basin from velocity modeling of multichannel seismic data, *Earth Planet. Sci. Lett.*, *259*, 239–255, doi:10.1016/j.epsl.2007.04.021.

Kappel, E. S., and W. B. F. Ryan (1986), Volcanic episodicity and a non-steady state rift valley along the northeast Pacific spreading centers: Evidence from Sea MARC I, *J. Geophys. Res.*, *91*, 13,925–13,940, doi:10.1029/JB091iB14p13925.

Kong, L. S. L., S. C. Solomon, and G. M. Purdy (1992), Microeartquake characteristics of a mid-ocean ridge along-axis high, *J. Geophys. Res.*, *97*, 1659–1685, doi:10.1029/91JB02566.

Lavier, L. L., and W. R. Buck (2002), Half graben versus large-offset low-angled normal fault: Importance of keeping cool during normal fault, *J. Geophys. Res.*, *107*(B6), 2122, doi:10.1029/2001JB000513.

Lawson, K., R. C. Searle, P. Browning, and P. Kempton (1996), Detailed volcanic geology of the MARNOK area, Mid-Atlantic Ridge, north of Kane transform, in *Tectonic, Magmatic, Hydrothermal and Biological Segmentation of Mid-Ocean Ridges*, edited by C. J. Macleod et al., *Geol. Soc. London Spec. Publ.*, *118*, 6–102.

Lin, J., and E. M. Parmentier (1989), Mechanisms of lithospheric extension at mid-ocean ridges, *Geophys. J.*, *96*, 1–22, doi:10.1111/j.1365-246X.1989.tb05246.x.

Lin, J., and M. Parmentier (1990), A finite amplitude necking model of rifting in brittle lithosphere, *J. Geophys. Res.*, *95*, 4909–4923, doi:10.1029/JB095iB04p04909.

Lin, J., and J. Phipps Morgan (1992), The spreading rate dependence of three-dimensional mid-ocean ridge gravity structure, *Geophys. Res. Lett.*, *19*, 13–16, doi:10.1029/91GL03041.

Macdonald, K. C. (1982), Mid-ocean ridges: Fine scale tectonic volcanic and hydrothermal processes within the plate boundary zone, *Annu. Rev. Earth Planet. Sci.*, *10*, 155–190, doi:10.1146/annurev.ea.10.050182.001103.

Macdonald, K. C. (1986), The crest of the Mid-Atlantic Ridge: Models for crustal generation processes and tectonics, in *The Western North Atlantic Region*, *Geol. of N. Am.*, vol. M, edited by P. R. Vogt and B. E. Tucholke, pp. 51–68, Geol. Soc. of Am., Boulder, Colo.

Maclennan, J., T. Hulme, and S. C. Singh (2004), Thermal models of oceanic crustal accretion: Linking geophysical, geological, and petrological observations, *Geochem. Geophys. Geosyst.*, *5*, Q02F25, doi:10.1029/2003GC000605.

Madsen, J. A., D. W. Forsyth, and R. S. Detrick (1984), A new isostatic model for the East Pacific Rise Crest, *J. Geophys. Res.*, *89*, 9997–10,015, doi:10.1029/JB089iB12p09997.

Magde, L. S., R. S. Detrick, G. M. Kent, A. J. Harding, J. A. Orcutt, J. C. Mutter, and P. Buhl (1995), The crustal and upper mantle contribution to the axial gravity anomaly at the southern East Pacific Rise, *J. Geophys. Res.*, *100*, 3747–3766, doi:10.1029/94JB02869.

Martinez, F., B. Taylor, E. T. Baker, J. A. Resing, and S. L. Walker (2006), Opposing trends in crustal thickness and spreading rate along the back-arc Eastern Lau Spreading Center: Implications for controls on ridge morphology, faulting, and hydrothermal activity, *Earth Planet. Sci. Lett.*, *245*, 655–672, doi:10.1016/j.epsl.2006.03.049.

Michael, P. J., et al. (2003), Magmatic and amagmatic seafloor generation at the ultraslow-spreading Gakkel ridge, Arctic Ocean, *Nature*, *423*, 956–961, doi:10.1038/nature01704.

Perfit, M. R., and W. W. J. Chadwick (1998), Magmatism at mid-ocean ridges: Constraints from volcanological and geochemical investigations, in *Faulting and Magmatism at Mid-Ocean Ridges*, *Geophys. Monogr. Ser.*, vol. 106, edited by R. Buck et al., pp. 59–115, AGU, Washington, D. C.

Phipps Morgan, J., and Y. J. Chen (1993a), Dependence of ridge-axis morphology on magma supply and spreading rate, *Nature*, *364*, 706–708, doi:10.1038/364706a0.

Phipps Morgan, J. P., and Y. J. Chen (1993b), The genesis of oceanic crust: Magma injection, hydrothermal circulation, and crustal flow, *J. Geophys. Res.*, *98*, 6283–6297, doi:10.1029/92JB02650.

Pockalny, R. A., R. S. Detrick, and P. J. Fox (1988), Morphology and tectonics of the Kane Transform from SeaBeam bathymetry data, *J. Geophys. Res.*, *93*, 3179–3193, doi:10.1029/JB093iB04p03179.

Poliakov, A. N. B., and W. R. Buck (1998), Mechanics of stretching elastic-plastic-viscous layers: Applications to slow-spreading mid-ocean ridges, in *Faulting and Magmatism at Mid-Ocean Ridges*, *Geophys. Monogr. Ser.*, vol. 106, edited by R. Buck et al., pp. 305–323, AGU, Washington, D. C.

Qin, R., and W. R. Buck (2005), Effect of lithospheric geometry on rift valley relief, *J. Geophys. Res.*, *110*, B03404, doi:10.1029/2004JB003411.

Shah, A. K., and W. R. Buck (2001), Causes for axial high topography at mid-ocean ridges and the role of crustal thermal structure, *J. Geophys. Res.*, *106*, 30,865–30,879, doi:10.1029/2000JB000079.

Singh, S. C., W. C. Crawfor, H. Carton, T. Seher, V. Combier, M. Cannat, J. P. Canales, D. Dusunur, J. Escartin, and J. M. Miranda (2006), Discovery of a magma chamber and faults beneath a Mid-Atlantic Ridge hydrothermal field, *Nature*, *442*, 1029–1032, doi:10.1038/nature05105.

Sinton, J. M., and R. S. Detrick (1992), Mid-ocean ridge magma chambers, *J. Geophys. Res.*, *97*, 197–216, doi:10.1029/91JB02508.

Sinton, J., E. Bergmanis, K. Rubin, R. Batiza, T. K. P. Gregg, K. Gronvold, K. C. Macdonald, and S. M. White (2002), Volcanic eruptions on mid-ocean ridges: New evidence from the superfast spreading East Pacific Rise, 17°–19°S, *J. Geophys. Res.*, *107*(B6), 2115, doi:10.1029/2000JB000090.

Sinton, J., R. Detrick, J. P. Canales, G. Ito, and M. Behn (2003), Morphology and segmentation of the Western Galapagos spreading center, 90.5°–98°W: Plume-ridge interactions at an intermediate spreading ridge, *Geochem. Geophys. Geosyst.*, *4*(12), 8515, doi:10.1029/2003GC000609.

Smith, D. K., and J. R. Cann (1990), Hundreds of small volcanoes on the median valley floor of the Mid-Atlantic Ridge (24°–30°N), *Nature*, *348*, 152–155, doi:10.1038/348152a0.

Solomon, S. C., P. Y. Huang, and L. Meinke (1998), The seismic moment budget of slow spreading ridges, *Nature*, *334*, 58–60.

Tapponnier, P., and J. Francheteau (1978), Necking of the lithosphere and the mechanics of slowly accreting plate boundaries, *J. Geophys. Res.*, *83*, 3955–3970, doi:10.1029/JB083iB08p03955.

Tolstoy, M., A. J. Harding, and J. A. Orcutt (1997), Deepening of the axial magma chamber on the southern East Pacific Rise toward the Garrett Fracture Zone, *J. Geophys. Res.*, *102*, 3097–3108, doi:10.1029/96JB03226.

Toomey, D. R., S. C. Solomon, and G. M. Purdy (1988), Microearthquakes beneath the median valley of the Mid-Atlantic Ridge near 23°N: Tomography and tectonics, *J. Geophys. Res.*, *93*, 9093–9112, doi:10.1029/JB093iB08p09093.

Toomey, D. R., S. C. Solomon, and G. M. Purdy (1994), Tomographic imaging of the shallow crustal structure of the East Pacific Rise at 9°30′N, *J. Geophys. Res.*, *99*, 24,135–24,157, doi:10.1029/94JB01942.

Tucholke, B. E., and J. Lin (1994), A geological model for the structure of ridge segments in slow spreading ocean crust, *J. Geophys. Res.*, *99*, 11,937–11,958, doi:10.1029/94JB00338.

Turcotte, D. L., and G. Schubert (2002), *Geodynamics*, 2nd ed., 456 pp., Cambridge Univ. Press, New York.

Vera, E. E., and J. B. Diebold (1994), Seismic imaging of oceanic layer 2A between 9°30′N and 10°N on the East Pacific Rise from two-ship wide-aperture profiles, *J. Geophys. Res.*, *99*, 3031–3041, doi:10.1029/93JB02107.

Wang, X., and J. R. Cochran (1993), Gravity anomalies, isostasy, and mantle flow at the East Pacific Rise crest, *J. Geophys. Res.*, *98*, 19,505–19,531, doi:10.1029/93JB01551.

Weiland, C. M., and K. C. Macdonald (1996), Geophysical study of the East Pacific Rise 15°–17°N: An unusually robust segment, *J. Geophys. Res.*, *101*, 20,257–20,274, doi:10.1029/96JB01756.

Wessel, P., and W. H. F. Smith (1995), New version of the Generic Mapping Tools released, *Eos Trans. AGU*, *76*(33), 329, doi:10.1029/95EO00198.

Wolfe, C. J., G. M. Purdy, D. R. Toomey, and S. C. Solomon (1995), Microearthquake characteristics and crustal velocity structure at 29°N on the Mid-Atlantic Ridge: The architecture of a slow spreading ridge, *J. Geophys. Res.*, *100*, 24,449–24,472, doi:10.1029/95JB02399.